学位論文（要約）

Polycrystal anelasticity at near-solidus temperatures: Experiments and seismological applications

（融点近傍における多結晶体の非弾性：実験と地震学的応用）

平成29年12月博士（理学）申請

東京大学大学院理学系研究科
地球惑星科学専攻

山内　初希

Abstract

Seismic low velocity and high attenuation observed in the upper mantle have been mostly attributed to the presence of melt. However, a recent experimental study on a polycrystalline aggregate showed that anelastic relaxation increases as temperature approaches the solidus temperature, indicating that seismic low velocity and high attenuation can occur without melt. In this previous study, because the experiment was performed only below the solidus temperature, the relationship between the increase of anelastic relaxation below the solidus temperature and partial melting was not clarified. The present study aimed to clarify the effects of temperature and partial melting on polycrystal anelasticity. For this purpose, the mechanical properties of a polycrystalline aggregate existing over a broad range of frequencies (elasticity, anelasticity, and viscosity) were measured at near-solidus temperatures ranging from below to above the solidus temperature (T_m).

The present experimental results show that the effects of partial melting on the mechanical properties of a polycrystalline material are twofold; changes just below the solidus temperature in the absence of melt and changes at the solidus temperature due to the onset of partial melting. Just below the solidus temperature ($0.92 \sim< T/T_m < 1$), anelastic relaxation significantly increases with increasing homologous temperature (T/T_m). Also, viscosity of the grain boundary diffusion creep is reduced significantly in this temperature range. At the solidus temperature ($T/T_m = 1$), further reduction of elasticity, further increase of anelastic relaxation strength, and further reduction of viscosity occur. The mechanical properties of a partially molten aggregate are determined by the total of these twofold changes.

The changes just below the solidus temperature are caused by a solid state mechanism, whereas the changes at the solidus temperature are caused by the direct effect of melt. I speculate that a structural transition at grain boundary occurs just before partial melting (premelting), which may change the dynamical properties of grain boundary and enhance grain boundary sliding (anelasticity) and grain boundary diffusion creep (viscosity). The present experimental result showed that the changes due to the premelting has a large amplitude even for a sample which generates a very small amount of melt (0.4–0.5%) at the solidus temperature, whereas the changes due to the direct effect of melt are very

small for a sample with very small melt fraction. The present result predicts that in most part of the upper mantle, where the melt fraction is considered to be very small, the direct effect of melt is negligibly small and the premelting effect is dominant.

To assess the effect of premelting on the seismic waves, I performed the parameterization of the present experimental results and obtained a general empirical formula for polycrystal anelasticity and viscosity. It was fitted to the temperature dependence of seismic shear wave velocity (V_S) in the Pacific mantle. The present model explains well the steep reduction of V_S just below the solidus temperature by the premelting effect without invoking any direct effect of melt. In the fitting, the material parameters (elasticity and viscosity) of the mantle rock needed to calculate V_S were determined as the fitting parameters. The obtained parameters agree well with those experimentally measured for olivine aggregates. By using the empirical formula and the material parameters determined by the fitting, a new anelasticity model applicable to the mantle was established.

The new anelasticity model was further applied to the lithosphere-asthenosphere boundary (LAB) to examine whether the premelting effect can explain the seismic discontinuity. Vertical structure of V_S was calculated, by using the geotherm obtained from the cooling models of oceanic plate and the solidus temperature of peridotite obtained from the thermodynamic models. The result shows that if the solidus temperature is decreased by the existence of volatile, seismic discontinuity is reproduced as the steep reduction of V_S by the premelting effect. In addition, the premelting effect can explain high attenuation in the asthenosphere. The present study proposes a new insight that premelting is the origin of the asthenosphere.

Contents

Chapter 1

Introduction

1.1 Importance of Understanding Anelasticity

At high temperatures, rock is a viscoelastic material which behaves elastically at high frequencies and viscously at low frequencies (Figure 1.1). Anelasticity is a transitional property between elasticity and viscosity, and causes dispersion and attenuation of the elastic waves [e.g., *Nowick and Berry*, 1972]. Therefore, it is important to understand rock anelasticity for a quantitative interpretation of the upper mantle seismic structures [e.g., *Karato*, 1993].

In the past, effects of temperature and pressure on the elastic properties of the rock forming minerals were investigated by using the ultrasonic method [e.g., *Isaak*, 1992]. Seismic frequency ($f = 10^{-3}$–1 Hz) is much lower than the ultrasonic frequency ($f >\sim 1$ MHz), and seismic waves can be affected by the rock anelasticity (Figure 1.1). However, in the 1980s and 90s, rock anelasticity had not received much attention, because one-dimensional global seismic structures, like PREM [*Dziewonski and Anderson*, 1981], can be almost fully explained by the ultrasonic data, or in other words, intrinsic elasticity of each mineral and its pressure and temperature dependence (e.g., anharmonic effect) [e.g., *Duffy and Anderson*, 1989]. Although the absorption band model was introduced to explain seismic attenuation [*Anderson and Given*, 1982], it was treated as a mere similitude.

Recent seismic tomographic studies have revealed the 2-D or 3-D structures of seismic wave velocity V and attenuation Q^{-1} in the upper mantle with high resolution [e.g., *Priestley and McKenzie*, 2013; *Nakajima et al.*, 2013; *Abers et al.*, 2014]. The lateral variations in V and Q^{-1} reflect the lateral heterogeneities in temperature, chemical composition (major and minor elements), grain size, and melt fraction. In particular, low-V

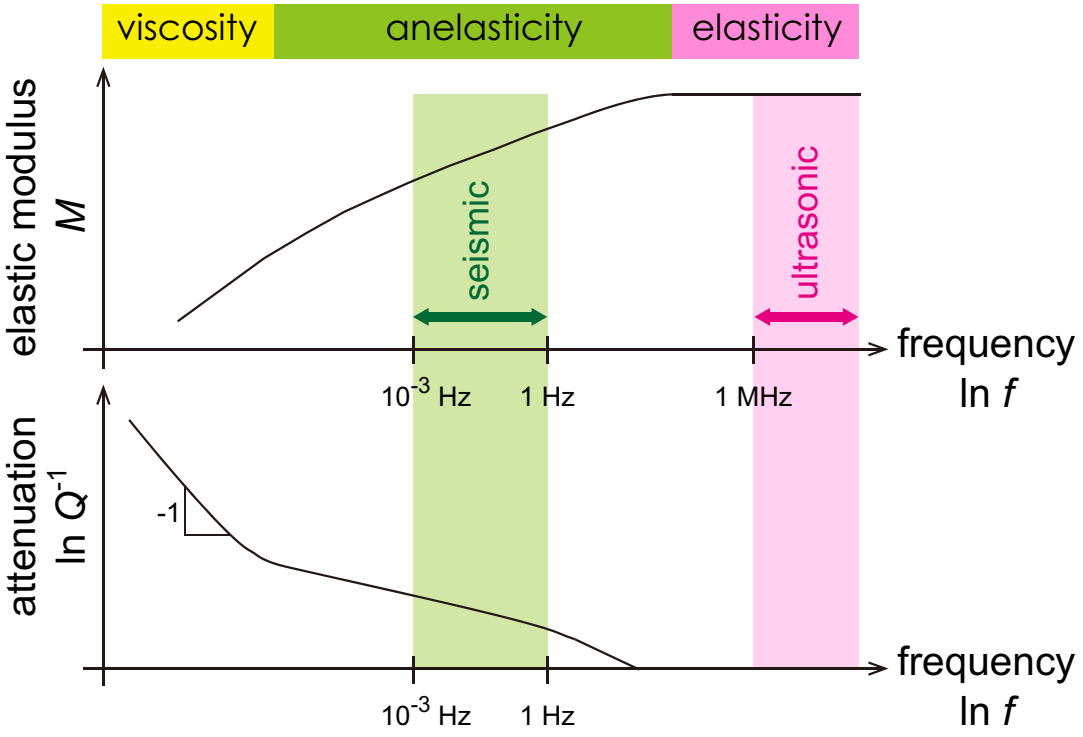

Figure 1.1: Schematic illustration for elastic modulus and attenuation for a viscoelastic material as functions of frequency. No dispersion and no attenuation in the elastic regime, and $Q^{-1} \propto f^{-1}$ in the viscous regime. Hatched areas by pink and green show the ultrasonic ($f >\sim 1$ MHz) and seismic ($f = 10^{-3}$–1 Hz) frequency ranges, respectively.

and high-Q^{-1} regions captured beneath the volcanic areas near the ridge and subduction zone have attracted much attention, and there were many attempts to constrain temperature, melt fraction, and/or water content in these regions [e.g., *Nakajima et al.*, 2005, 2013]. However, effects of these factors measured at MHz–GHz cannot solely explain the seismological data in a consistent manner with the other geophysical and geochemical constraints. Understanding rock anelasticity especially at near-solidus temperatures is necessary for quantitative interpretation of such seismic anomalies [*Takei et al.*, 2014; *Abers et al.*, 2014]. In order to update the understanding of anelasticity as required by the recent progress of seismology, measurement of rock anelasticity at seismic frequencies has become crucial [e.g., *Jackson et al.*, 2002].

1.2 Previous Experimental Studies of Polycrystal Anelasticity

Forced oscillation tests have been performed on the mantle rock samples to investigate the effects of temperature, grain size, chemical composition, and melt on the rock anelasticity [e.g., *Gribb and Cooper,* 1998; *Tan et al.*, 2001; *Jackson et al.*, 2002, 2004; *Barnhoorn*

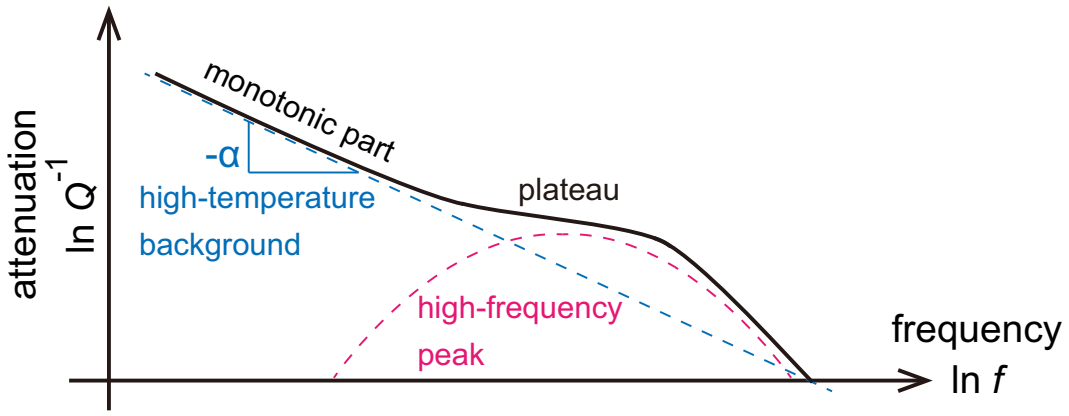

Figure 1.2: (black) Schematic illustration for the typical form of the attenuation spectrum observed in the forced oscillation tests for rock and rock analogue. The attenuation spectrum is represented by the superposition of high-temperature background (blue) and high-frequency peak (pink).

et al., 2007; *Jackson and Faul*, 2010]. However, the data obtained so far are not enough to understand the underlying mechanism which is necessary to extrapolate the experimental data to the mantle conditions. To address this lack, forced oscillation tests on the rock analogue (polycrystalline aggregates of organic "borneol") have been performed [*McCarthy et al.*, 2011; *McCarthy and Takei,* 2011; *Takei et al.*, 2014]. The attenuation spectra obtained from the rock and rock analogue generally consist of a monotonic part ($Q^{-1} = Q_0^{-1} f^{-\alpha}$, $\alpha = 0.2$–0.3) observed at low frequencies and a plateau or flattening observed at high frequencies (Figure 1.2, black line). Here, I review how these parts have been understood in the previous studies.

1.2.1 Monotonic Part (High-temperature Background)

The monotonic part, which is called "high-temperature background", has been observed robustly in all experiments (Figure 1.2, blue dashed line). Particularly, in the early experiments for the mantle rocks, only this part was captured [*Gribb and Cooper,* 1998; *Tan et al.*, 2001; *Jackson et al.*, 2002]. At that time, rock anelasticity was treated under the assumption of similitude; by using a single master variable f/f_r, attenuation spectra obtained under various experimental conditions (e.g., temperature T, grain size d, and pressure P) were expressed as $Q^{-1}(f, T, d, P) = Q^{-1}(f/f_r)$, where $f_r(T, d, P)$ represents the reference frequency. By clarifying the dependence of f_r on temperature, grain size, and/or pressure, the underlying mechanism for anelasticity have been investigated. The samples in these early experiments do not include melt nor many dislocations. Therefore,

the dissipation was attributed to the grain boundary sliding (GBS).

Gribb and Cooper [1998] first proposed the idea of Maxwell frequency scaling. Maxwell frequency is calculated as $f_M = M_U/\eta$ by using the unrelaxed elastic modulus M_U and the viscosity η of grain boundary diffusion creep. They showed that when anelasticity is induced by diffusionally accommodated GBS [*Raj and Ashby*, 1971; *Raj*, 1975], attenuation spectrum can be expressed as $Q^{-1}(f/f_M)$ by using a single master variable f/f_M. This is intuitively understandable because GBS is rate limited by matter diffusion along the grain boundaries in the same manner as grain boundary diffusion creep [*Raj*, 1975]. Another mechanism of GBS, called elastically accommodated GBS, has a reference frequency f_e different from f_M [*Raj and Ashby*, 1971]. The most remarkable difference between f_e and f_M is in the grain size dependence ($f_e \propto d^{-1}$ [e.g., *Nowick and Berry*, 1972], and $f_M \propto d^{-3}$). Therefore, in order to test the Maxwell frequency scaling, the grain size dependence of f_r has to be investigated. *Gribb and Cooper* [1998], however, investigated only the temperature dependence of Q^{-1}. *Jackson et al.* [2002] measured Q^{-1} and η for various temperatures and grain sizes. Although the obtained temperature and grain size dependence of f_r agreed well with those of f_M, the grain size dependence of f_r and f_M was d^{-1}, which was different from the theoretical prediction (d^{-3}). *Morris and Jackson* [2009] further investigated the applicability of the Maxwell frequency scaling to the data of *Jackson et al.* [2002] by using η extrapolated from other data set. However, they could not obtain a conclusive result because of a large uncertainty in η.

To investigate the applicability of the Maxwell frequency scaling, anelasticity data with reliable viscosity data are required. *McCarthy et al.* [2011] accurately measured both anelasticity and viscosity of rock analogue (borneol) under various temperatures and grain sizes. They showed that the attenuation spectra obtained under various experimental conditions collapse onto a single curve, when the testing frequency f is normalized to the Maxwell frequency f_M (Figure 1.3, black symbols). Their viscosity data (and hence f_M) show the grain size exponent of 3. Furthermore, they showed that the data for melt-free olivine aggregates collapse onto the same master curve, demonstrating the universality of the master curve for polycrystalline materials. *McCarthy and Takei* [2011] further showed that Q^{-1} data for melt-bearing borneol samples collapse onto the master curve as melt-free samples.

In Figure 1.3, the shaded frequency range ($f/f_M = 10^6$–10^9) corresponds to the seismic

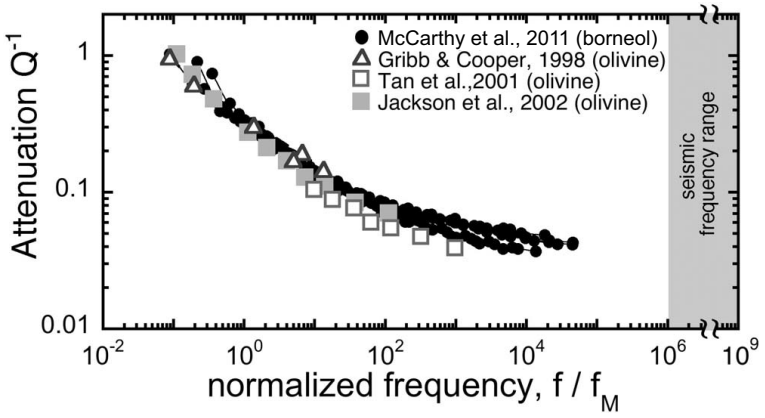

Figure 1.3: Measured Q^{-1} versus normalized frequency f/f_M (after *McCarthy et al.* [2011], modified). Black symbols show data for borneol aggregates (at T = 22.4–45.4°C and d = 3.4–22 μm) [*McCarthy et al.*, 2011], and the others are data for olivine aggregates. For *Gribb and Cooper* [1998], T = 1200 and 1250°C; d = 3 μm. For *Tan et al.* [2001], T = 1200°C; d = 23.6 μm. For *Jackson et al.* [2002], T = 1200°C; d = 2.9 μm. The shaded area shows the normalized seismic frequency range.

range ($f = 10^{-3}$–1 Hz) normalized to the f_M of the upper mantle ($f_M = M_U/\eta \simeq 10^{11}$ Pa/10^{20} Pas = 10^{-9} Hz). All experimental data existing at that time did not cover the seismic range. The understanding of anelasticity at higher frequencies became crucial for seismological applications. The subsequent experiments for the mantle rock [e.g., *Jackson et al.*, 2004; *Jackson and Faul*, 2010] and for the rock analogue [*Takei et al.*, 2014] found a plateau in the higher-frequency part of the attenuation spectra, as reviewed in subsection 1.2.2.

1.2.2 Plateau (High-frequency Peak)

Attenuation spectrum with a plateau is usually represented by the superposition of the high-temperature background and a broad peak existing at high normalized frequencies ($f/f_M \gg 1$) [*Jackson et al.*, 2004; *Jackson and Faul*, 2010; *Takei et al.*, 2014]. The broad peak causing the plateau is hereafter referred to as "high-frequency peak" (Figure 1.2, pink dashed line). In order to clarify the mechanism of the high-frequency peak, experimental studies to investigate the scaling law have been performed. Although there is a general consensus about the mechanism of the high-temperature background, that of the high-frequency peak is still controversial. It is crucial to better understand the high-frequency peak, because it dominates the attenuation in the seismic frequency range [*Takei et al.*, 2014].

Generally, the high-frequency peak is small for melt-free rocks [*Jackson and Faul*, 2010] and large for melt-bearing rocks [*Jackson et al.*, 2004; *Sundberg and Cooper*, 2010].

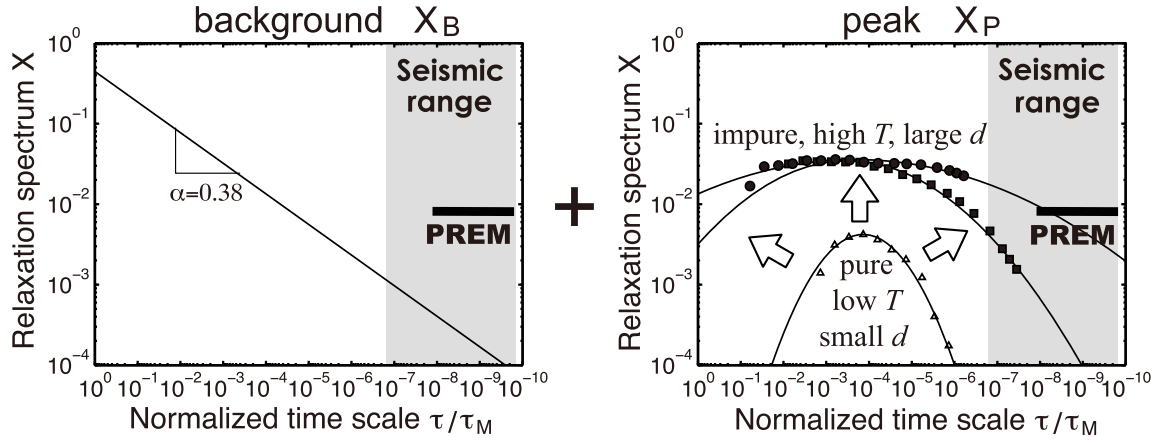

Figure 1.4: Relaxation spectra for high-temperature background (background X_B) and for high-frequency peak (peak X_P) are plotted as functions of time scale normalized to the Maxwell relaxation time τ/τ_M (adapted from *Takei et al.* [2014]). In the right plot, some experimental data of X_P (symbols) and their best fit Gaussian distribution (solid lines) are shown. Solid symbols show data for the impure borneol samples (at $T = 10$–20°C ($T/T_m = 0.90$–0.93) and $d = 19$–23 μm), and open for the high-purity borneol sample (at $T = 5$°C ($T/T_m = 0.58$) and $d = 4.4$ μm), where T_m is solidus or melting temperature. Attenuation can be approximately calculated from $X(= X_B + X_P)$ as $Q^{-1}(f/f_M) \simeq \pi/2 \times X(\tau/\tau_M = f_M/(2\pi f))$, where $\tau_M = f_M^{-1}$.

Recent data obtained from the rock analogue showed the amplitude and width of the peak increase with increasing temperature and grain size (Figure 1.4) [*Takei et al.*, 2014]. *Takei et al.* [2014] considered this result as an important clue to understand the mechanism for the large high-frequency peak in the partially molten rocks.

Takei et al. [2014] used high-purity borneol and impure borneol containing diphenylamine. The high-frequency peak captured for the impure borneol sample was significantly larger than that captured for the high-purity borneol sample at the same temperature T and grain size d. Because the impurity (diphenylamine) lowers the solidus temperature T_m, this observation can be interpreted that the high-frequency peak increases as temperature approaches the solidus. Similar observation was reported for rock samples; high-frequency peak was large for a lower-purity MgO sample but undetectable for a high-purity MgO sample [*Webb and Jackson*, 2003; *Barnhoorn et al.*, 2007]. *Takei et al.* [2014], therefore, speculated that the high-frequency peak is mutually related to "partial melting" and might be scaled by using the homologous temperature T/T_m. However, their data were limited to the sub-solidus temperatures ($T/T_m \leq 0.93$). To understand the effect of partial melting on the high-frequency peak, it is needed to observe the peak continuously from subsolidus to supersolidus temperatures. The significant enhancement of the high-frequency peak at subsolidus temperatures suggests the possibility of low V

and high Q^{-1} even without melt in the upper mantle [*Takei et al.*, 2014]. To apply the experimental results to the upper mantle and discuss the causes of the seismic low V and high Q^{-1}, it is necessary to obtain an experimental formula by the parameterization of the experimental data extending from subsolidus to supersolidus temperatures.

1.3 Purpose of This Study and Structure of This Thesis

The purposes of this study are summarized as follows:

- To clarify the effects of temperature and partial melting on the high-frequency peak
- To complete the parameterization of the high-frequency peak and obtain an empirical model of polycrystal anelasticity
- To apply the experimentally obtained anelasticity model to the seismic waves and assess the effect of anelasticity on the seismic structures in the upper mantle

I achieved these goals by conducting the experiments on polycrystal anelasticity at near-solidus temperatures ranging from subsolidus to supersolidus temperatures and applying the results to the seismological data. This thesis consists of five chapters. The experimental study is shown in Chapter 2, and the applications are shown in Chapters 3–4. Contents of each chapter are as follows:

Chapter 2: Detailed methods and results of the experiment and discussion on the mechanism of the high-frequency peak. The work presented in this chapter has been published as *Yamauchi, H., and Y. Takei (2016), Polycrystal anelasticity at near-solidus temperatures, J. Geophys. Res. Solid Earth, 121, 7790–7820.*

Chapter 3: Parameterization of the experimental data and its applicability test to the mantle. The work presented in this chapter has been also published as *Yamauchi, H., and Y. Takei (2016), Polycrystal anelasticity at near-solidus temperatures, J. Geophys. Res. Solid Earth, 121, 7790–7820.* As part of this research, the fitting of the new anelasticity model to the seismological data was conducted by co-author Y. Takei (section 3.2).

Chapter 4: Application of the new anelasticity model obtained in Chapter 3 to the seismic discontinuity at the oceanic lithosphere-asthenosphere boundary. The manuscript

for the work presented in this chapter is in preparation and intended for submission to the *Journal of Geophysical Research: Solid Earth* as the title *Application of new anelasticity model to seismic discontinuity at lithosphere-asthenosphere boundary* (tentative).

Chapter 5: Overall conclusions of this thesis are presented.

Chapter 2

Experimental Study of Polycrystal Anelasticity at Near-Solidus Temperatures

I measured the anelasticity of the rock analogue at near-solidus temperatures ranging from subsolidus to supersolidus temperatures ($0.89 \leq T/T_m \leq 1.01$) and investigated the effect of temperature and partial melting on the high-frequency peak. Using the same rock analogue used in the previous studies [*McCarthy et al.*, 2011; *McCarthy and Takei*, 2011; *Takei et al.*, 2014], I performed the forced oscillation test to measure the anelasticity from 100 Hz to 2×10^{-4} Hz, the creep test to measure the steady state viscosity, and the ultrasonic test to measure the unrelaxed elastic modulus. The measured viscosity and unrelaxed elastic modulus were used to calculate the Maxwell frequency f_M. The anelasticity data obtained in this study were limited to $f/f_M \leq 10^6$, because viscosity is low, and hence, f_M is high at near-solidus temperatures. However, the total relaxation strength of the high-frequency peak can be estimated by using the deficit of the modulus measured by the forced oscillation test from the unrelaxed modulus. Although the anelasticity of the same material at the subsolidus and supersolidus temperatures was reported by *McCarthy and Takei* [2011], the modulus data of the forced oscillation test in this previous study were not accurate enough to quantitatively estimate the total relaxation of the high-frequency peak. The accuracy of the modulus data was greatly improved by the new forced oscillation apparatus and pore-free samples developed by *Takei et al.* [2014]. Using the improved methods by *Takei et al.* [2014], I obtained a new data set which enables a detailed examination of the high-frequency peak at near-solidus temperatures.

2.1 Experimental Details

2.1.1 Sample Preparation

Borneol ($C_{10}H_{18}O$; melting temperature = 204.5°C) is classified as a plastically crystalline organic that deforms by the same kinds of diffusion and dislocation processes as minerals, metals, and ceramics [*Sherwood*, 1979]. Aggregates of borneol + melt obtained by partially melting the samples made from borneol + diphenylamine ($(C_6H_5)_2NH$) binary eutectic system (eutectic temperature $T_m = 43$°C, Figure 2.1a) have an equilibrium microstructure similar to that of olivine + basalt system [*Takei*, 2000]. Therefore, high-purity borneol and borneol + diphenylamine system have been used as rock analogue to investigate the mechanical properties of melt-free and melt-bearing polycrystalline materials [*Takei*, 2000; *McCarthy et al.*, 2011; *McCarthy and Takei*, 2011; *Takei et al.*, 2014]. In this study, elasticity, anelasticity, and viscosity of the borneol + diphenylamine system were measured from below to above the eutectic temperature, and the onset of melting was examined in a broad frequency range. In this chapter, unless otherwise specified, T_m represents the eutectic temperature of the binary samples, 43°C, which is also referred to as solidus temperature.

Eight samples used in this study are summarized in Table 2.1. Samples #40–44 were used in the forced oscillation test and creep test, and samples #h10–h12 and a half-cut piece of #42 were used in the ultrasonic test. A sample without diphenylamine is referred to as high-purity borneol. Samples made from borneol + 0.833 wt%, 1.666 wt%, and 3.332 wt% diphenylamine are referred to as BD1, BD2, and BD4, respectively, because they can produce 1 wt%, 2 wt%, and 4 wt% melt, respectively, at $T = T_m$ (Figure 2.1a). The difference between weight fraction and volume fraction of melt is negligible because the density of melt (1.051×10^3 kg/m^3) is almost equal to that of borneol (1.011×10^3 kg/m^3) [*Takei*, 2000].

Following *Takei et al.* [2014], very fine powder (~ 3 μm) of high-purity borneol or a mixture of borneol and diphenylamine, obtained from a cold-ball milling procedure (−40°C, 6 days), was placed in a cylindrical die and pressed to 13.9 MPa at room temperature for about 4 days to produce fully dense, polycrystalline right circular cylinders (diameter $2R = 30$ mm; length $L = 65$ mm for the forced oscillation test and $L = 25$ mm for the ultrasonic test). Before removing the sample from the die, isothermal an-

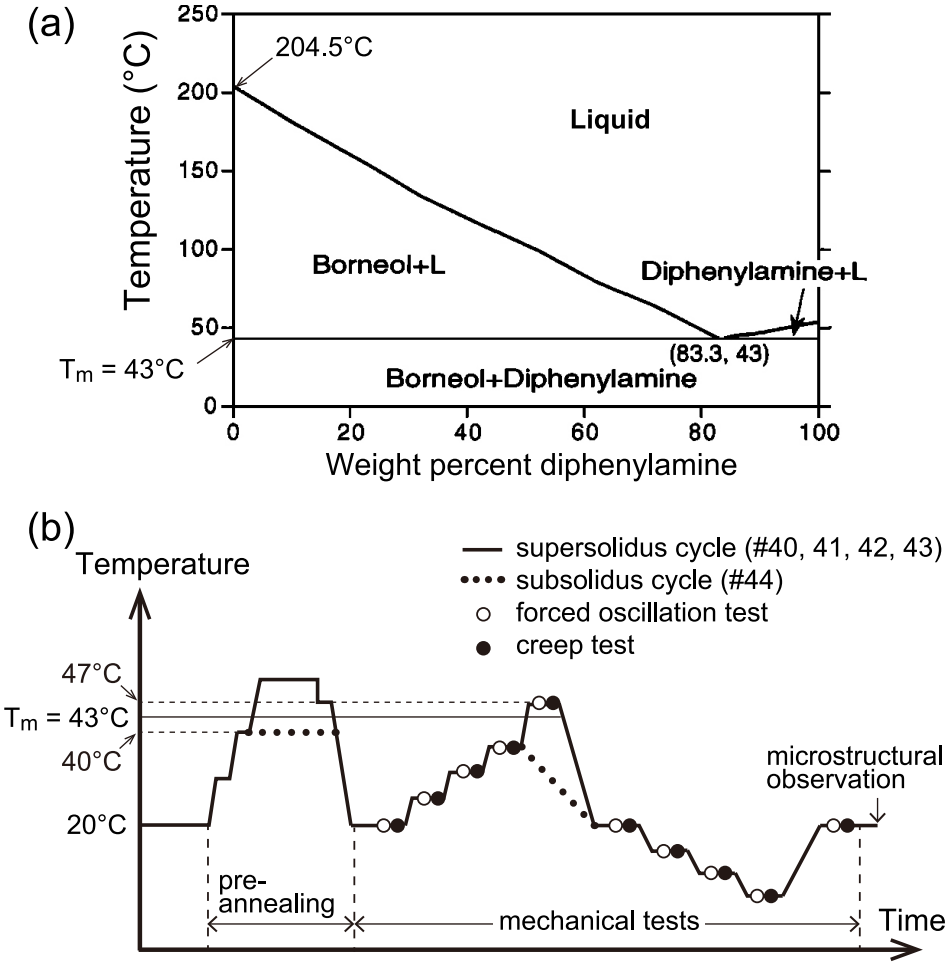

Figure 2.1: (a) Phase diagram of borneol + diphenylamine binary eutectic system (after *Takei* [2000], modified). Data from *D'Ans et al.* [1964]. (b) Typical thermal histories of a supersolidus cycle (thick solid line) and a subsolidus cycle (thick dotted line).

Table 2.1: Experimental Samples Used in This Study

Sample Number	Initial Chemical Composition	Preannealing (°C) [(days)]	Melt Fraction[g] ϕ	Grain Size d (μm)	Density ρ (10^3 kg/m^3)	Voidage[h] (%)
40[a]	BD1[c]	30[1];40[1];47[4]	0.0045 ± 0.0017	24.4 ± 1.2	1.0044	0.7
41[a]	BD1[c]	30[1];40[1];55[7.7];47[1]	0.0040 ± 0.0003	34.2 ± 1.5	1.0072	0.4
43[a]	BD1[c]	30[1];40[1];55[50];47[2]	0.0054 ± 0.0003	39.7 ± 0.4	1.0073	0.4
42[a,b]	BD2[d]	30[1];40[1];55[7.7];47[1]	0.0162 ± 0.0002	46.3 ± 1.1	1.0064	0.6
44[a]	BD2[d]	30[1];40[15]	0.02	12.5 ± 0.4	1.0063	0.7
h10[b]	BD4[e]	30[1];40[1];55[9];47[1]	0.0059 ± 0.0010	48.7 ± 2.1	1.0087	0.3
h12[b]	BD4[e]	30[1];40[1];55[5];47[1]	0.0272 ± 0.0014	58.4 ± 3.3	1.0082	0.6
h11[b]	high purity[f]	30[1];40[1];55[5]	0	18.8 ± 1.3	1.0058	0.5

[a] Used in the forced oscillation test and creep test.
[b] Used in the ultrasonic test.
[c] Borneol + 0.833 wt % diphenylamine.
[d] Borneol + 1.666 wt % diphenylamine.
[e] Borneol + 3.332 wt % diphenylamine.
[f] High-purity borneol.
[g] Melt fraction generated at 43°C is shown. Not in percent.
[h] Calculated from the density of borneol (1.011×10^3 kg/m^3) and that of diphenylamine (1.160×10^3 kg/m^3) [*Takei*, 2000].

nealing was performed at elevated pressure ($\sim$ 3 MPa) and temperatures (30–55°C) for a duration summarized in Table 2.1. In order to minimize the grain growth during the mechanical testing, the annealing temperature was higher than the highest run temperature of each sample. Binary sample #44 was annealed below T_m (hereafter referred to as subsolidus annealing), whereas the other binary samples were annealed above T_m, that is, in a partially molten state (supersolidus annealing). Equilibrium dihedral angle θ of the borneol + melt system depends on temperature [*Takei*, 2000]. Therefore, at the end of the supersolidus annealing, temperature was kept at 47°C for more than one day, so that the equilibrium melt geometry corresponding to $\theta = 34.6°$ develops. After the high-temperature annealing, the sample was removed from the die; a teflon inner sleeve allowed removal of the sample without fracture. The initial sample geometry (diameter $2R$ and length L) was measured accurately with micrometers. The sample mass was also measured accurately. From the measured geometry and mass, density ρ and voidage were calculated.

In the supersolidus annealing, a piston and a bottom rod with O-rings were used to avoid the escape of melt from the sample. When removed from the die, the piston and rod were caked with a small amount of solidified melt, which was squeezed into the gaps between the sample and O-rings during the supersolidus annealing. Therefore, the mass of the escaped melt was estimated accurately by measuring the incremental mass of these parts. Then, the melt fraction ϕ of each sample at $T = T_m$ (Table 2.1) was calculated from the initial chemical composition and the mass of the escaped melt. Error in ϕ comes from the uncertainty in the escaped melt mass. (A large amount of melt (3.41%) escaped from the sample #h10 accidentally during the supersolidus annealing.)

2.1.2 Measurement of Anelasticity and Viscosity

Anelasticity and viscosity were measured for samples #40–44 by using the forced oscillation apparatus developed by *Takei et al.* [2014]. After attaching two brass end platens, the sample and platens were sealed in a non-reactive plastic bag to prevent sublimation and evaporation during the mechanical testing. The sample was then attached to the forced oscillation apparatus (Figure 2.2) by clamping the two end platens tightly to the mirrored sample head and the bottom plate using a platen-clamping system (Figure 1c in *Takei et al.* [2011]). We removed air from all contact planes of the plastic bag against

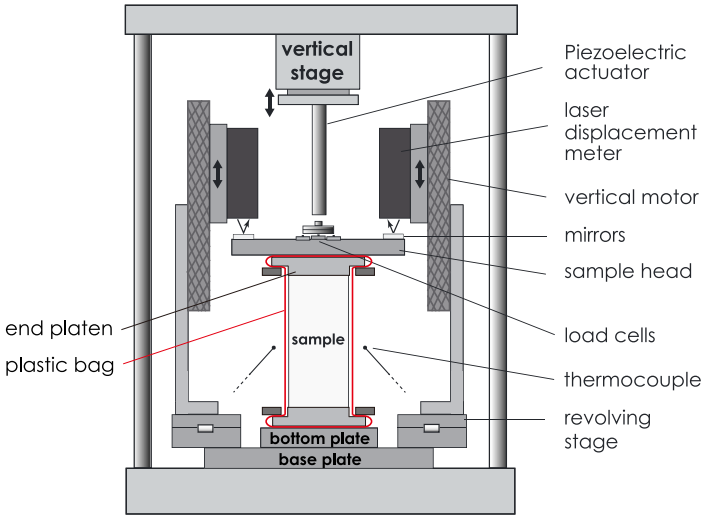

Figure 2.2: Schematic illustration of the forced oscillation apparatus used in this study (after *Takei et al.* [2014], modified). Sample and two brass end platens, which are sealed in a non-reactive plastic bag, are tightly fixed to the apparatus. The apparatus is placed within a temperature-controlled chamber, and the temperature is monitored by two thermocouples that terminate in air approximately 5 mm from the sample.

the two end platens, sample head, and bottom plate, by using epoxy bonding agent and superglue. The sample was first deformed at about 30°C for several days under a uniaxial stress (0.11 MPa) to ensure good contact with the two end platens. Then, anelasticity and steady state viscosity were measured at various run temperatures. Typical temperature cycles are shown in Figure 2.1b. There are two types of cycles. Samples #40–43 were pre-annealed at supersolidus temperatures and tested both below and above the solidus temperature to investigate the effect of partial melting (thick solid line in Figure 2.1b). This type of cycle is referred to as supersolidus cycle. In contrast, sample #44 was pre-annealed at subsolidus temperature and tested near, but only below, the solidus temperature (thick dotted line in Figure 2.1b). This is called subsolidus cycle. Forced oscillation test and creep test were performed at each run temperature (open and solid circles in Figure 2.1b). In the forced oscillation test, a series of sinusoidal stress (zero-to-peak amplitude $\simeq$ 0.03 MPa), in addition to an offset stress (0.11 MPa), was applied, and Young's modulus E and attenuation Q^{-1} were measured at various frequencies from 68.1 Hz to 2.15×10^{-4} Hz. After a long run with 14–19 frequencies (primary run), a short run with less than ten frequencies was repeated to check the reproducibility (repeated run). In the creep test, a steady-state viscosity was measured under the constant offset stress. Further details of these tests are presented in *Takei et al.* [2014]. The amplitude

of the offset stress and that of the sinusoidal stress were smaller than those in *Takei et al.* [2014], because the run temperatures of this study are higher and hence the samples had lower viscosity.

When all mechanical tests were finished, the testing sample was cut in half perpendicularly to the cylindrical axis. The cross section was polished to a mirror finish with a microtome and examined with a high-resolution real color confocal microscope (Lasertec Optelics C130). Sample #42 was cut in half without damage, and one piece ($L \simeq 30$ mm) was used for the measurement of ultrasonic velocities.

The data obtained from the forced oscillation tests and the creep tests were processed in the same manner as described previously [*Takei et al.*, 2014]. Young's modulus E and attenuation Q^{-1} were obtained from the amplitude ratio σ_0/ε_0 and the tangent of phase delay δ, respectively, between the uniaxial stress and strain. Complex compliance is also calculated as $J^* = J_1 + iJ_2 = (\varepsilon_0/\sigma_0)e^{i\delta}$. Phase delay δ was corrected for the instrumental time lags, and Young's modulus E was corrected for the effects of apparatus stiffness and sample length (Appendices A1–A3 in *Takei et al.* [2014]). The apparatus compliance C_a^* used in the correction was measured by a blank test with a stainless-steel sample which was superglued to the two brass end platens, sealed in a plastic bag, and then fixed to the apparatus in exactly the same manner as the experimental samples. The apparatus compliance C_a^* ($\mathrm{Re}(C_a^*) \simeq 1 \times 10^{-9}$ m/N, $\mathrm{Im}(C_a^*) \simeq 2 \times 10^{-11}$ m/N) was slightly larger than that in *Takei et al.* [2014] due to the plastic bag and was highly reproducible. *Takei et al.* [2014] estimated the random and systematic errors of the E measurement by the present forced oscillation apparatus to be $< 2\%$ and $\leq\sim 3\%$, respectively, by using the deficit Δ_∞ from the unrelaxed Young's modulus E_U (section 3.5 in *Takei et al.* [2014]). This estimate applies to the present data as well. Viscosity η was calculated from the constant offset stress σ_{offset} and the steady-state uniaxial creep rate $\dot{\varepsilon}$ as $\eta = \sigma_{\mathrm{offset}}/\dot{\varepsilon}$.

Rigorously speaking, attenuation measured by the uniaxial test should be written as Q_E^{-1}, which is generally affected by both bulk Q_K^{-1} and shear Q_μ^{-1} attenuation. However, because of a large Poisson's ratio of borneol ($\nu = 0.371$ [*Takei*, 2000]), even if $Q_K^{-1} \simeq Q_\mu^{-1}$, the contribution from Q_K^{-1} to Q_E^{-1} is negligible, and hence $Q_E^{-1} \simeq Q_\mu^{-1}$ [*McCarthy et al.*, 2011]. Viscosity of the uniaxial deformation, η_E, is related to the shear viscosity η_μ as $\eta_E = 3\eta_\mu$. In this study, Q_E^{-1} and η_E are simply written as Q^{-1} and η, respectively.

2.1.3 Measurement of Ultrasonic Velocity

Longitudinal and shear wave velocities, V_P and V_S, of samples #h10–h12 and #42 were measured by using ultrasonic waves. Each sample was sealed in a bag made of nonreactive plastic film (thickness = 77 μm) to avoid sublimation and evaporation during the measurement. The sample assembly is given in Figure 2 of *Takei* [2000]. Both P and S travel times were measured by the pulse transmission method by using PS-dual transducers (D7054, Panametrics Inc., center frequency = 1 MHz). The measurement was performed at various temperatures in a constant temperature chamber. The temperature cycle was similar to that of the supersolidus cycle in Figure 2.1b. Sample length L was measured accurately at each run temperature by using a micrometer. Further details of the measurement are presented in *Takei et al.* [2014]. After the ultrasonic tests, microstructural observation to measure grain size was performed on the testing samples.

Following *Takei et al.* [2014], the obtained travel times were corrected for the time lags caused by the transducers and by the plastic films. Possible errors in V_P and V_S data are ± 0.15% and ± 0.2%, respectively [*Takei et al.*, 2014]. For a partially molten sample, however, high-frequency components of the shear waves dissipate significantly, and the possible error in V_S is estimated to be ± 1%.

2.2 Results

2.2.1 Microstructure and Grain Size

Figure 2.3a shows the typical microstructure of the high-purity borneol sample (#h11), Figure 2.3b shows that of the binary sample used in the subsolidus cycle (#44), and Figures 2.3c and 2.3d show those of the binary samples used in the supersolidus cycle (#42 and #41, respectively). In the samples used in the supersolidus cycle, the solidified melt pockets were observed homogeneously at the triple junctions of the borneol grains (Figures 2.3c and 2.3d). Some pockets were also found along the grain boundaries as indicated by the white arrows in Figures 2.3c and 2.3d. In contrast, in the sample used in the subsolidus cycle, the grain-edge melt network was not observed but the diphenylamine grains with similar sizes as borneol grains existed homogeneously, as indicated by the black arrows in Figure 2.3b. This remarkable difference between Figure 2.3b and Figures 2.3c–2.3d confirms that the binary samples are not partially molten below the eutectic temperature 43°C, as expected from the phase diagram (Figure 2.1a).

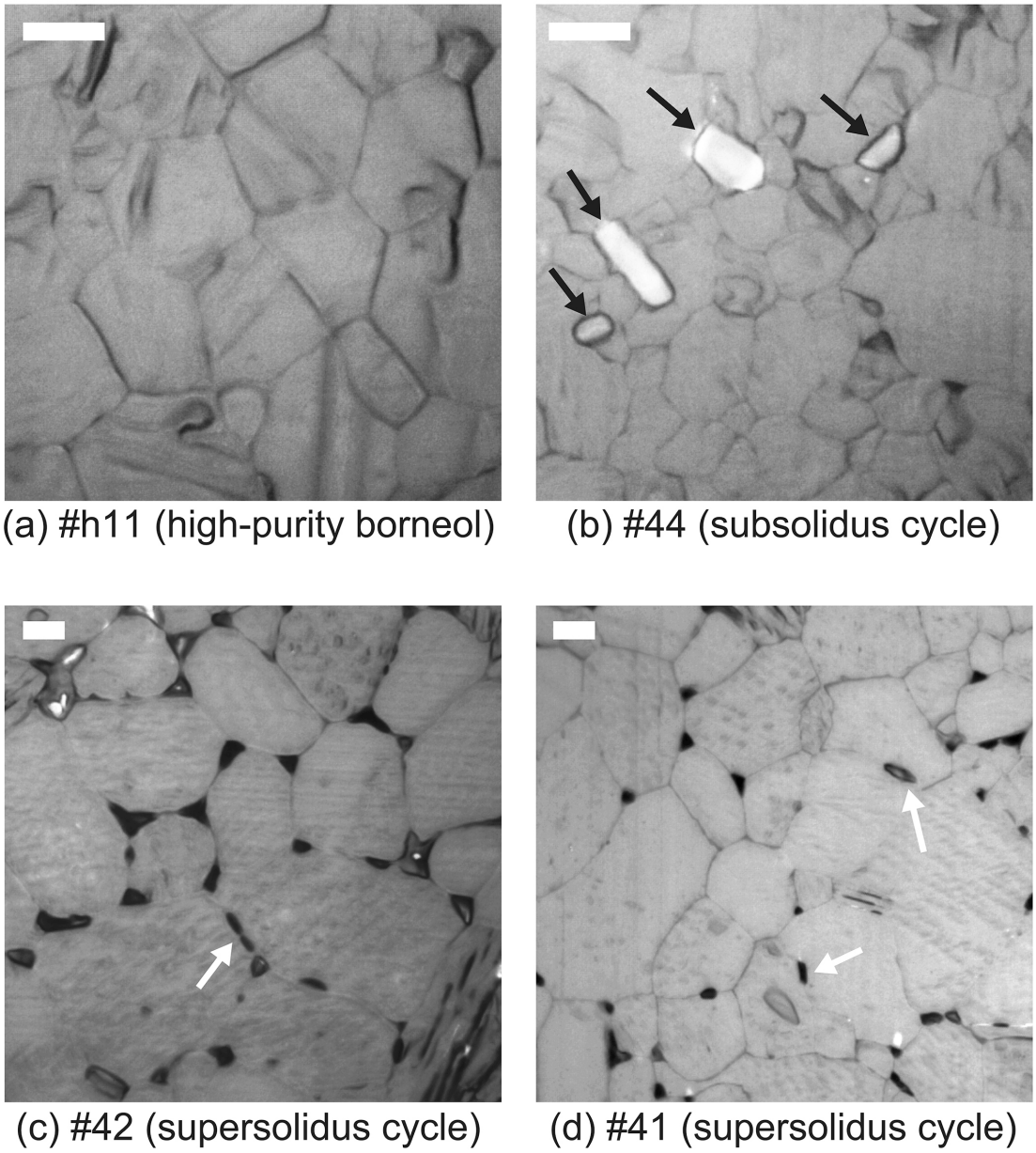

Figure 2.3: Light microscope images of (a) high-purity borneol (#h11) and (b, c, d) borneol + diphenylamine samples, where (b) sample #44 was used in the subsolidus cycle (thick dotted line in Figure 2.1b) and (c, d) samples #42 and #41 were used in the supersolidus cycle (thick solid line in Figure 2.1b). Black arrows in Figure 2.3b show diphenylamine grains. Melt pockets in Figures 2.3c ($\phi = 1.6\%$) and 2.3d ($\phi = 0.4\%$) are exaggerated by preferential sublimation at the melt-grain interface. White arrows in Figures 2.3c and 2.3d show the isolated melt pockets along the grain boundaries. In all figures, scale bar is 10 μm.

Mean grain size was measured by the line intercept method with a factor of 1.5 [*Gifkins,* 1970]. The measurement was conducted at several positions for each sample, and the averages of the measured grain sizes are summarized in Table 2.1 with one sigma uncertainty of the average. As shown in section 2.2.3, viscosity is sensitive to the grain size ($\eta \propto d^m, m \simeq 3$). Viscosity at ∼23°C measured at the end of each temperature cycle was almost equal to that measured at the beginning, and hence the grain size of each sample can be considered as constant (Viscosity shows $d_{\rm end}/d_{\rm beginning} \simeq 1.0$–$1.05$ for samples #40–43, and $\simeq 1.2$ for #44).

2.2.2 Ultrasonic Velocity

Figure 2.4 shows the typical waveforms obtained at the subsolidus (dashed line) and supersolidus (solid line) temperatures. Velocity reduction and attenuation by partial melting are considerably larger for the shear wave than for the longitudinal wave. The Fourier transformation of the waveforms shows that the testing frequency of the P wave is $f \simeq 1$ MHz at all temperatures, and that of the S wave is $f \simeq 1$ MHz at subsolidus temperatures but $f \simeq 700$ kHz at supersolidus temperatures.

Figure 2.5 shows V_P and V_S obtained for samples #h10–h12 and #42 as functions of temperature. Solid symbols show the warming stage, and open symbols show the subsequent cooling stage. This figure clearly shows that, compared with the high-purity sample (#h11), the binary samples (#h10, 42, h12) have considerably lower V_P and V_S at the supersolidus temperatures ($\geq$ 43°C). These velocity reductions, which increase with increasing melt fraction, can be attributed to the partial melting. The reduction was initiated at about 8°C lower than T_m in the warming stage. These observations are

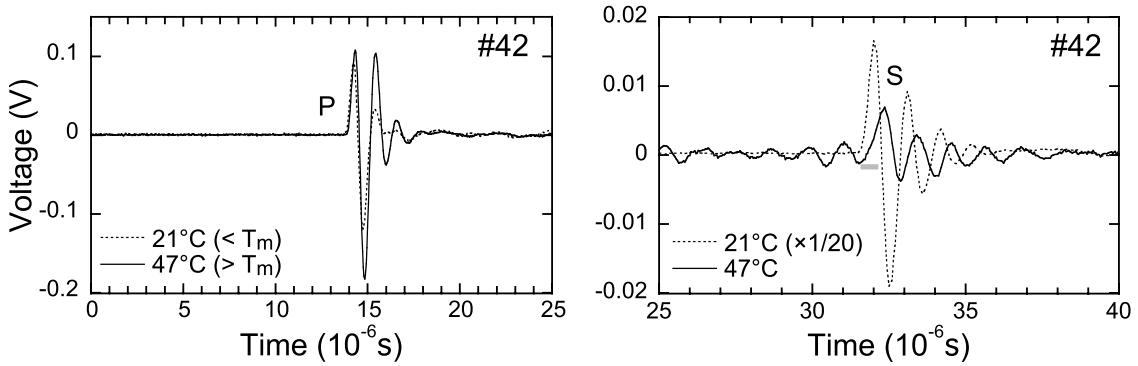

Figure 2.4: Ultrasonic waveforms of sample #42 at 21°C ($< T_m$) and 47°C ($> T_m$, partially molten). (left) Longitudinal waves. (right) Shear waves, where voltage for $T = 21$°C is reduced to one-twentieth, and gray bar shows the reading error for 47°C ($\pm$ 0.21 μs corresponding to $\pm$ 0.64% error to V_S).

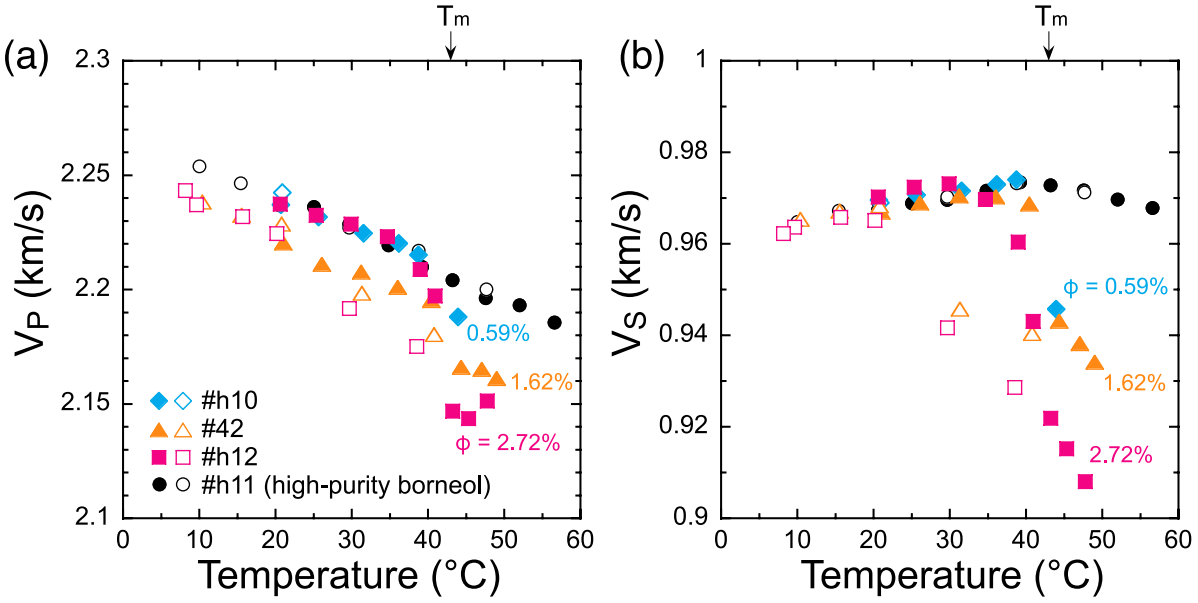

Figure 2.5: Temperature dependence of (a) longitudinal and (b) shear wave velocities obtained from the ultrasonic measurements. Each sample is denoted by color and symbol shape, where solid symbols show the warming stage and open symbols show the subsequent cooling stage. All samples except for the high-purity sample (#h11) are partially molten at $T \geq T_m$ (= 43°C), and the numerals near the data symbols show the melt fraction in the same color.

consistent with the results of *Takei* [2000]. Hysteresis was observed for samples #42 and #h12; in the solidifying stage of melt, velocity was lower and attenuation was higher than those in the warming stage. However, these samples regained the initial high velocity and low attenuation finally after sufficient cooling below 20°C.

When temperature is more than 8°C lower than T_m (and without the hysteresis), V_P and V_S are insensitive to the chemical composition and grain size (Figure 2.5), showing that anelastic relaxation does not occur at the frequencies higher than the ultrasonic frequency ($f \geq 1$ MHz). We, therefore, calculated the unrelaxed Young's modulus E_U by using V_P, V_S, and density ρ of the high-purity sample (#h11). Figure 2.6 shows the obtained $E_U(T)$, which shows good agreement with the previous result by *Takei et al.* [2014]. As discussed in *Takei et al.* [2014], the slight increase in E_U with increasing T (< 40°C) is considered to be an intrinsic property of borneol.

Figure 2.7 shows V_P/V_P^0 and V_S/V_S^0 of the partially molten samples as functions of melt fraction ϕ, where V_P^0 and V_S^0 are the velocities of the melt-free sample (#h11) at the same temperature. Also shown in Figure 2.7 are the predictions from the theory of poroelasticity (dashed and solid lines):

$$\frac{V_P}{V_P^0} = \frac{\sqrt{K_{\text{eff}}/k + (4\gamma/3)N/\mu}}{\sqrt{1+4\gamma/3}\sqrt{\bar{\rho}/\rho}}, \tag{2.1}$$

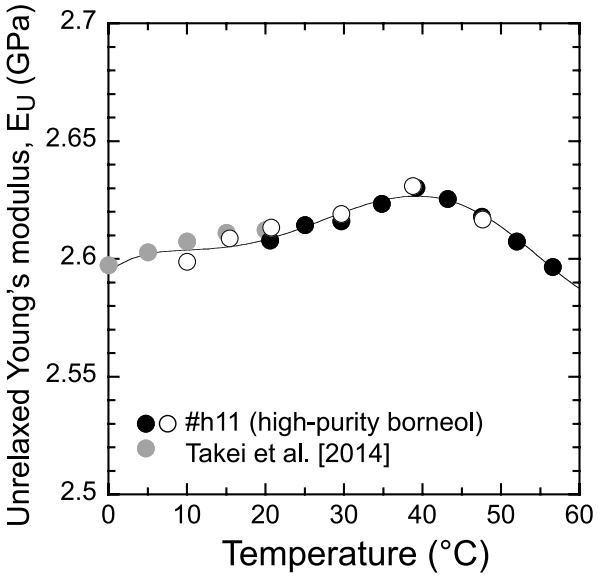

Figure 2.6: Unrelaxed Young's modulus $E_{\rm U}$ calculated from V_P, V_S, and ρ of the high-purity borneol sample (#h11). Solid symbols show the warming stage (20°C $\rightarrow$ 60°C) and open symbols show the cooling stage (60°C $\rightarrow$ 10°C). Black line shows the best fit curve given by $E_{\rm U}(T) = \sum_{k=0}^{k=5} a_k T^k$, where T is temperature in °C, $a_0 = 2.5943$, $a_1 = 2.6911 \times 10^{-3}$, $a_2 = -2.9636 \times 10^{-4}$, $a_3 = 1.4932 \times 10^{-5}$, $a_4 = -2.9351 \times 10^{-7}$, and $a_5 = 1.8997 \times 10^{-9}$. Gray symbols show the previous data (U35BD1S in *Takei et al.* [2014]).

$$\frac{V_S}{V_S^0} = \frac{\sqrt{N/\mu}}{\sqrt{\bar{\rho}/\rho}}, \tag{2.2}$$

and

$$\frac{K_{\rm eff}}{k} = \frac{K_b}{k} + \frac{(1 - K_b/k)^2}{1 - \phi - K_b/k + \phi k/k_f} \tag{2.3}$$

[e.g., *Biot*, 1956; *Takei*, 2002]. Parameters μ, k, and ρ are the shear modulus, bulk modulus, and density, respectively, of the solid phase, and $\gamma = \mu/k$. Parameters k_f and ρ_f are the bulk modulus and density, respectively, of the melt phase, and $\bar{\rho} = (1-\phi)\rho + \phi\rho_f$. Parameters K_b and N are the bulk and shear moduli of the solid skeleton, which are given as functions of porosity (= melt fraction) ϕ and dihedral angle θ [*Takei,* 1998]. The solid and dashed lines in Figure 2.7 were calculated from equations (2.1)–(2.3) by using the Poisson's ratio of borneol ($\nu = 0.371$), the density ratio between borneol and melt ($\rho_f/\rho = 1.04$), the compressibility ratio between borneol and melt (k/k_f =1.16), and the dihedral angle $\theta = 34.6°$ [*Takei*, 2000]. Equations (2.1)–(2.3) give the relaxed state of the melt squirt flow in which the testing frequency is low enough to allow melt to flow between the connected pores [*Mavko and Nur*, 1975]. The good agreement between the data and the theory shows that the partially molten samples are almost in the relaxed state of the melt squirt flow at the ultrasonic frequency ($f \simeq 700$ kHz).

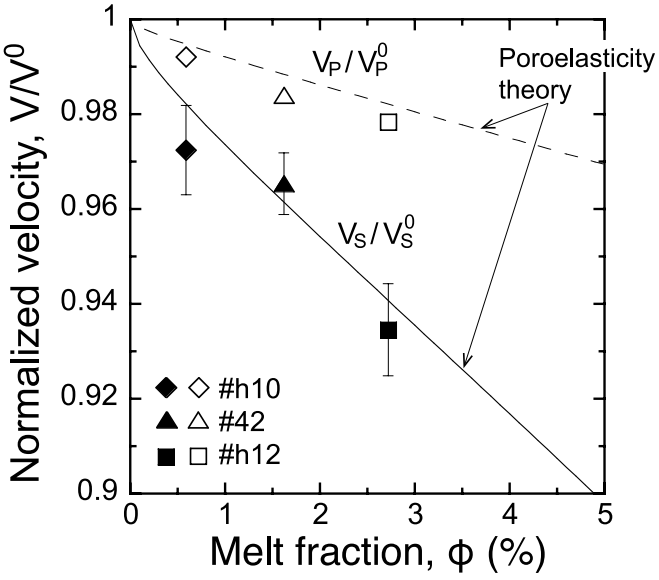

Figure 2.7: Ultrasonic velocities of the partially molten samples ($T = 44$°C for #h10, 47°C for #42, and 48°C for #h12) normalized to those of the melt-free sample (V_S^0, V_P^0) are plotted as functions of melt fraction. Solid and open symbols show the measured V_S/V_S^0 and V_P/V_P^0, respectively. Solid and dashed lines show those predicted from the poroelasticity theory [*Takei*, 2000].

The ultrasonic result of the Young's modulus obtained in the partially molten state is hereafter written as E_U^ϕ. In this study, $E_U(T)$ and E_U^ϕ, representing the anharmonic and poroelastic effects, respectively, are used as the reference unrelaxed moduli to investigate the anelastic relaxations existing at lower frequencies, which are the primary focus of this study. Although the poroelastic effect was initiated at 8°C lower than T_m, E_U^ϕ is used only at $T \geq T_m$, for simplicity. This simplification does not affect the conclusions of this study, because the relaxations at frequencies lower than the ultrasonic frequency are much stronger than the poroelastic effect. Note that E_U^ϕ corresponds to the undrained modulus (eqs. (2.1)–(2.3)). The drained modulus would be better to evaluate the poroelastic effect at $f < 40$ Hz ($= k_\phi k_f / R^2 \eta_f \phi$ [e.g., *Cleary*, 1978; *Lu and Jackson*, 2006] with sample size $R = 15$ mm, permeability $k_\phi = d^2\phi^2/1600$, and melt viscosity $\eta_f = 7 \times 10^{-3}$ Pas). However, as shown later, the difference between the drained and undrained moduli is small.

2.2.3 Viscosity

Typical creep curves are shown in Figure 2.8. Because the constant offset stress was applied continuously, linear creep curves corresponding to the steady state were obtained. All viscosity data are summarized in Table 2.2 together with the detailed temperature

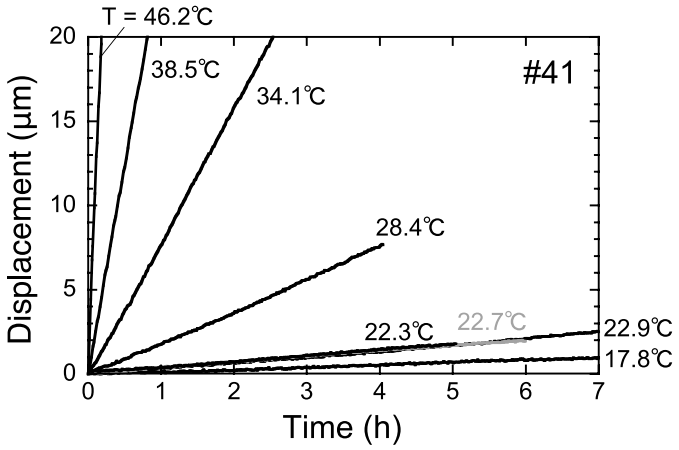

Figure 2.8: Typical creep curves (sample #41).

history of each sample. By fitting the formula

$$\eta(T, d, \phi) = Bd^m \exp\left(\frac{H}{RT}\right) \exp(-\lambda\phi) \tag{2.4}$$

to these results, grain size d dependence, temperature T dependence, and melt fraction ϕ dependence of viscosity are detailed in this section. We also show an anomalous behavior deviating from these systematics, which can be attributed to a hysteresis effect of the partial melting.

Figure 2.9a shows the viscosity at $T = 23 \pm 1°\mathrm{C}$ ($< T_m$) versus grain size, where data of our previous study are also plotted by gray symbols. Although these samples have various chemical compositions (corresponding to ϕ = 0.4–2% at T_m), all data, except for those shown by open symbols (#42 and the first temperature cycle of #43), collapse fairly well onto the regression line with a grain size exponent of $m = 2.56$. This result is supported by the result of *McCarthy and Takei* [2011] that the viscosity of the binary samples at subsolidus temperatures is insensitive to the concentration of diphenylamine. The grain size exponent $m(= 2.56)$ is close to 3, showing that the dominant mechanism for the steady-state creep is the grain boundary diffusion creep. Possible cause of the significant deviation of the data of #42 and of the first temperature cycle of #43 from the regression line is discussed below.

To elucidate temperature dependence, the viscosity data corrected for the grain size effect are shown in Figure 2.9b as a function of T^{-1}. Solid symbols in Figure 2.9b show the data obtained for samples #40, 41, 44, and for the second temperature cycle of #43, in the same symbol scheme as Figure 2.9a. The η versus T^{-1} curves for these samples bend sharply at $T \simeq 23°\mathrm{C}$, and the activation energy H is higher at $T \geq 23°\mathrm{C}$ than

Table 2.2: Viscosity Data

#40 ($d = 24.4$ μm)		#41 ($d = 34.2$ μm)		#42 ($d = 46.3$ μm)	
T[a] (°C)	η (10^{12} Pa s)	T[a] (°C)	η (10^{12} Pa s)	T[a] (°C)	η (10^{12} Pa s)
23.1 ± 0.7	22.1	22.9 ± 0.2	67.3	24.1 ± 0.3	13.4
28.9 ± 0.7	4.44	28.4 ± 0.3	12.9	29.9 ± 0.2	4.57
34.7 ± 0.6	0.941	34.1 ± 0.2	3.09	35.2 ± 0.2	1.81
39.2 ± 0.5	0.347	38.5 ± 0.2	1.03	39.4 ± 0.2	0.858
46.1 ± 0.2	0.104	46.2 ± 0.4	0.248	47.5 ± 0.3	0.203
23.5 ± 0.7	24.6	23.6 ± 0.2	6.24[c]	24.3 ± 0.3	16.6
18.3 ± 0.8	76.5	Cooling at 15°C		18.9 ± 0.4	55.5
13.4 ± 0.8	187	22.7 ± 0.2	72.9	13.2 ± 0.5	132
8.5 ± 0.7	(565)[b]	17.8 ± 0.2	167	24.1 ± 0.3	15.1
23.3 ± 0.8	21.7	13.0 ± 0.1	(497)[b]		
		8.2 ± 0.2	(1433)[b]		
		22.3 ± 0.1	69.3		

#43 ($d = 39.7$ μm)		#44 ($d = 12.5$ μm)	
T[a] (°C)	η (10^{12} Pa s)	T[a] (°C)	η (10^{12} Pa s)
First T cycle		22.6 ± 0.3	6.09
23.6 ± 0.3	34.5	28.3 ± 0.2	1.50
29.0 ± 0.3	7.84	34.5 ± 0.2	0.288
34.5 ± 0.3	2.73	38.7 ± 0.1	0.0918
39.0 ± 0.4	1.02	23.4 ± 0.3	10.1
46.5 ± 0.3	0.267	18.7 ± 0.3	32.1
Second T cycle		13.7 ± 0.6	109
23.8 ± 0.3	47.6	8.1 ± 0.7	258
18.3 ± 0.3	108	23.2 ± 0.5	10.6
13.5 ± 0.3	377		
28.9 ± 0.3	11.7		
33.9 ± 0.3	3.96		
38.6 ± 0.4	1.38		
46.3 ± 0.4	0.335		
23.6 ± 0.3	55.4		

[a] Run temperature $T = (T_1 + T_2)/2 \pm |T_1 - T_2|/2$, where T_1 and T_2 represent the temperatures of the two thermocouples (Figure 2.2).

[b] Value in the parentheses is estimated by using the fitting formula given by equation (2.4).

[c] A datum which is not used in Figures 2.8, 2.9, and Table 2.3.

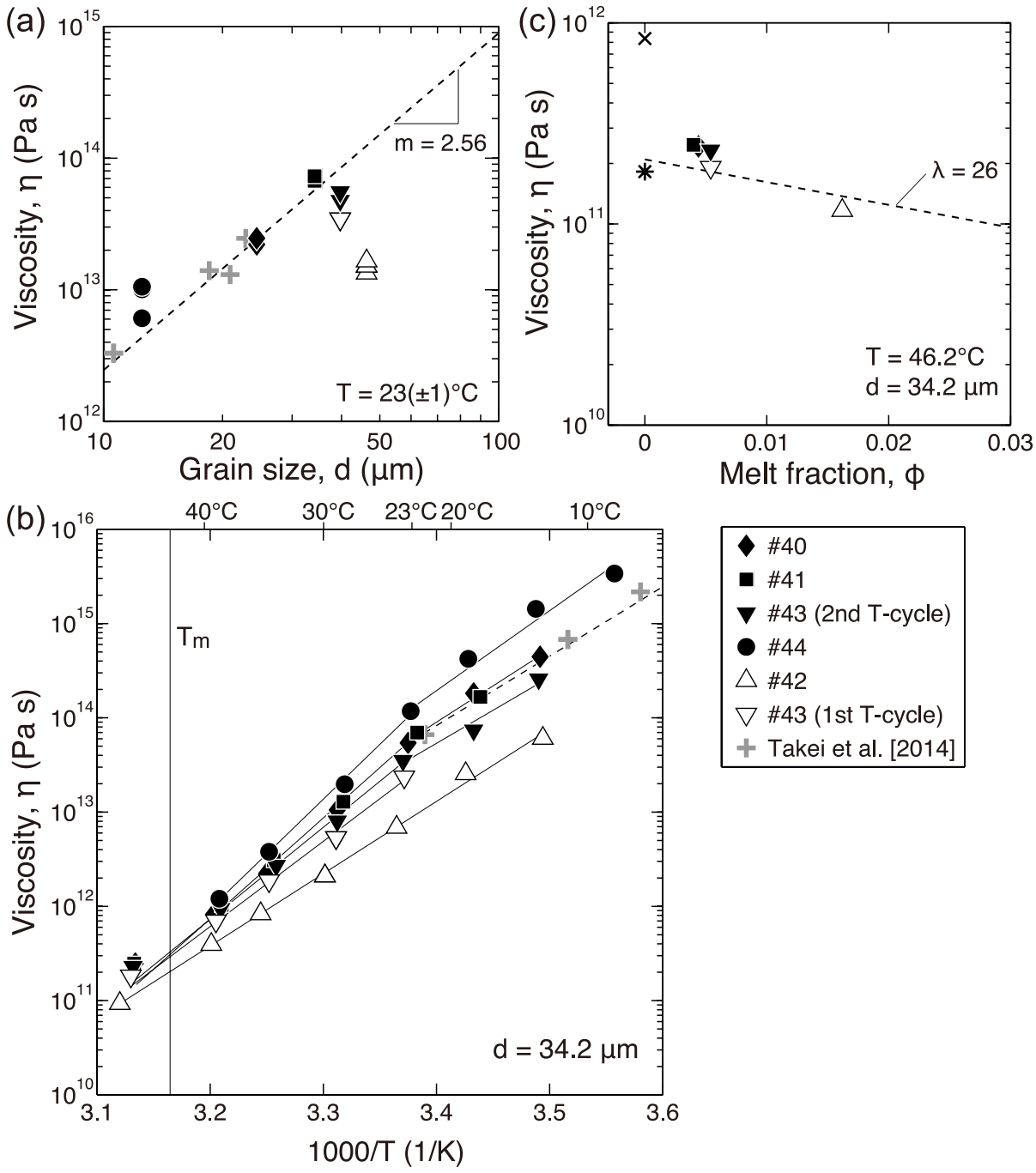

Figure 2.9: (a) Viscosity at $T = 23 \pm 1$°C ($< T_m$) versus grain size. (b) Viscosity corrected for the grain size effect versus inverse absolute temperature. (c) Viscosity at $T = 46.2$°C ($> T_m$) corrected for the grain size effect versus melt fraction ϕ. In the correction for the grain size, grain size exponent $m = 2.56$ and reference grain size $= 34.2$ μm were used. The data of this study are shown in black, where symbol shape shows each sample, and the data of the BD1 and BD2 samples in *Takei et al.* [2014] are shown in gray. Although each sample has multiple data points at 23°C (Figure 2.9a), only the average is shown in Figure 2.9b. In Figure 2.9c, the cross and asterisk symbols show η at $\phi = 0$ calculated from a typical value of η at 23°C (#41) by using $H = 205$ kJ/mol (asterisk) or 147 kJ/mol (cross), and the line shows the melt fraction dependence of $\exp(-\lambda\phi)$ with $\lambda = 26$ [*Mei et al.*, 2002].

Table 2.3: Activation Energy H Estimated from Viscosity Data

	H (kJ/mol)	
Sample Number	$T \leq 23$°C	23°C $\leq T < T_m$
40 and 41	147 ± 7	205 ± 3
43 (2nd T cycle)	134 ± 15	187 ± 6
44	162 ± 18	222 ± 16
42	147 ± 4	147 ± 4
43 (1st T cycle)	–	173 ± 8
Takei et al. [2014][a]	141 ± 3	–

[a] BD1 samples.

at $T \leq 23$°C. The low activation energy at $T \leq 23$°C (134–162 kJ/mol, Table 2.3) is consistent with the previous result obtained in the same temperature range (141 kJ/mol, *Takei et al.* [2014]). The high activation energy at $T \geq 23$°C (187–222 kJ/mol, Table 2.3) was newly recognized in this study. Such a bend in the Arrhenius plot does not exist in the high purity samples (Figure 8a in *Takei et al.* [2014]) and is characteristic of the binary samples at near solidus temperatures ($T/T_m \geq 0.94$).

Open symbols in Figure 2.9b show the data obtained for sample #42 and for the first temperature cycle of #43, which showed anomalously low viscosity in Figure 2.9a. As shown in Figure 2.9b, these samples did not show a high activation energy at $T \geq$ 23°C. Sample #43, however, regained a higher viscosity and a sharp bend in the second temperature cycle (solid inverted triangles), indicating that the anomalous behavior in the first cycle (open inverted triangles) was not an inherent property. Also, sample #41 showed a significantly low viscosity at 23°C just after the cooling from the partially molten state, but regained the high viscosity after further cooling at 15°C (Table 2.2). Therefore, such anomalous behavior in viscosity is, we think, a hysteresis effect of the partial melting. This hypothesis is supported from the fact that such anomaly in viscosity was not observed for the samples which had not experienced partial melting (sample #44 of this study and all binary samples in *Takei et al.* [2014]), nor observed for the partially molten samples, as shown in the next paragraph. In section 2.2.4, we will show that the hysteresis effect affecting the viscosity data also affect the anelasticity data.

The viscosity data under the partially molten condition, corrected for the grain size effect, are plotted in Figure 2.9c as a function of melt fraction ϕ. All data depend on ϕ systematically, showing that the samples do not exhibit any hysteresis in the partially molten state. The obtained dependence on ϕ is consistent with that of partially molten

rocks, which is usually represented as $\eta \propto e^{-\lambda\phi}$ with $\lambda = 25$–30 [*Mei et al.*, 2002; *Hirth and Kohlstedt*, 2003]. The viscosity at $\phi = 0$ (asterisk and cross symbols in Figure 2.9c) was calculated from the typical result of η at 23°C (#41), where the temperature effect from 23°C to 43°C was estimated by using either $H = 205$ kJ/mol (a typical value of H at $T \geq 23$°C) or $H = 147$ kJ/mol (a small value of H at $T \leq 23$°C). The asterisk symbol ($H = 205$ kJ/mol) lies on the smooth extension of the partially molten data, corresponding to the experimental result that η decreased continuously with increasing T even at $T = T_m$ (Figure 2.9b). The cross symbol ($H = 147$ kJ/mol) is used in the discussion section.

2.2.4 Young's Modulus and Attenuation

Typical examples of the Young's modulus E and attenuation Q^{-1} measured by the forced oscillation tests are shown in Figure 2.10 for #41 and #42. Results for the other samples can be found in Appendix A. Solid symbols show the data at subsolidus temperatures, and open symbols show those in the partially molten state. Young's modulus E generally decreases, and attenuation Q^{-1} generally increases with decreasing frequency and/or increasing temperature. Horizontal lines in Figures 2.10a and 2.10c indicate the levels of unrelaxed Young's modulus $E_U(T)$ obtained from the ultrasonic data at $f \sim 1$ MHz (Figure 2.6). The temperature dependence of E at $f < 100$ Hz is far stronger than that of E_U due to the occurrence of anelastic relaxation. Previous studies have shown that the anelasticity of polycrystalline aggregates follows the Maxwell frequency (f_M) scaling, particularly at low frequencies [e.g., *Takei et al.*, 2014]. We plot the obtained anelasticity data as a function of the normalized frequency f/f_M, and investigate a possible deviation from the Maxwell frequency scaling in detail.

The Maxwell frequency f_M for temperature T, grain size d, chemical composition C, and melt fraction ϕ was calculated by using the directly measured viscosity η as

$$f_M(T, d, C, \phi) = \frac{E_U(T)}{\eta(T, d, C, \phi)}. \tag{2.5}$$

Figures 2.11 and 2.12 show the normalized Young's modulus E/E_U and attenuation Q^{-1} as functions of the normalized frequency f/f_M. The data for sample #42 and the first temperature cycle of #43, both of which showed anomalously low viscosity due to the hysteresis effect of partial melting (section 2.2.3), are plotted in Figure 2.12, and the data for samples #40, 41, 44 and the second temperature cycle of #43, which did not exhibit

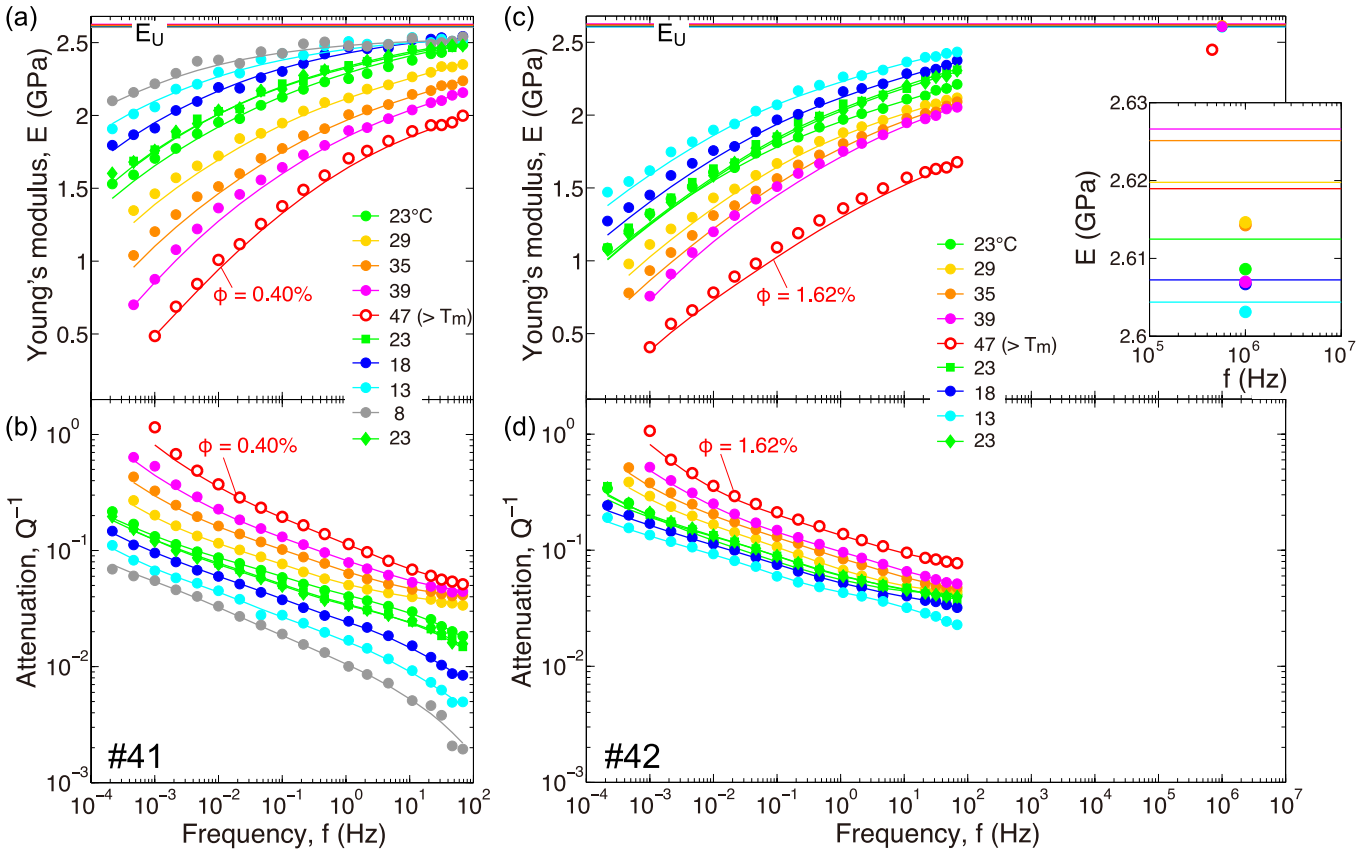

Figure 2.10: Typical examples of Young's modulus and attenuation measured by the forced oscillation tests are shown for samples (a, b) #41 and (c, d) #42 as functions of testing frequency f. Symbols show the experimental data, where each line shows the fitting using the corresponding relaxation spectrum in Figure 2.14. Color represents run temperature, where solid and open symbols show the data at subsolidus and supersolidus temperatures, respectively. The legend is arranged in the order of the measurements (from top to bottom). Horizontal lines in Figures 2.10a and 2.10c show the unrelaxed Young's modulus $E_U(T)$ (Figure 2.6) in the same color scheme. In Figure 2.10c, ultrasonic data for #42 are also plotted at $f = 1$ MHz for $T < T_m$ and at $f = 700$ kHz for $T > T_m$ with an enlarged view (insert).

the hysteresis in the viscosity data, are plotted in Figure 2.11.

We first examine Figure 2.11. The attenuation data (Figures 2.11b, 2.11d, 2.11f, and 2.11h) show that Q^{-1} collapses onto a nearly single curve at $f/f_M < 10^4$, but does not at $f/f_M > 10^4$; when $f/f_M > 10^4$, Q^{-1} corresponding to a given value of f/f_M increases with increasing temperature. The modulus data (Figures 2.11a, 2.11c, 2.11e, and 2.11g) show that E/E_U corresponding to a given value of f/f_M decreases with increasing temperature. This behavior of E/E_U can be explained well by the behavior of Q^{-1} at $f/f_M > 10^4$, because the reduction of E/E_U at a certain value of f/f_M is determined by the total relaxation strength at higher normalized frequencies than this f/f_M.

The anelasticity data in Figure 2.11 follow the Maxwell frequency scaling at $f/f_M < 10^4$, but do not at $f/f_M > 10^4$. In contrast, E/E_U and Q^{-1} shown in Figure 2.12 collapse onto each single master curve for all normalized frequencies except for the supersolidus data of sample #42. In particular, the collapse of the E/E_U data onto a nearly single curve means that the Q^{-1} data follow the Maxwell frequency scaling even at the high normalized frequencies where data points do not exist. The samples shown in Figure 2.12 are characterized by the anomalous behavior in viscosity, which was attributed to the hysteresis of partial melting (section 2.2.3). Therefore, the perfect applicability of the Maxwell frequency scaling is considered to be resulted from the hysteresis.

Without the hysteresis, the Maxwell frequency scaling is not fully applicable because of the tendency that the total relaxation strength at $f/f_M > 10^4$ increases with increasing temperature (Figure 2.11). This tendency was reported by *Takei et al.* [2014], in which only the subsolidus cycles were performed and hence the data are free from the hysteresis. Although the previous data were limited to $T/T_m \leq 0.93$, the present study confirmed that this tendency continues up to the supersolidus temperature.

The temperature dependences of anelasticity shown in Figures 2.10 (and A.1), 2.11, and 2.12 are mostly continuous even at the solidus temperature. A discontinuous change at the onset of partial melting was observed only in the E data of sample #42 with the largest melt fraction (Figures 2.10c and 2.12a). In other words, the discontinuous change in anelasticity at the onset of melting does not occur at small melt fractions ($\phi < 1\%$). Also shown in Figures 2.10c and 2.12a are the Young's modulus measured on this sample by using the ultrasonic waves (symbols at $f \sim 1$ MHz). These ultrasonic data show a discontinuity at the onset of melting, which can be explained well by the poroelastic

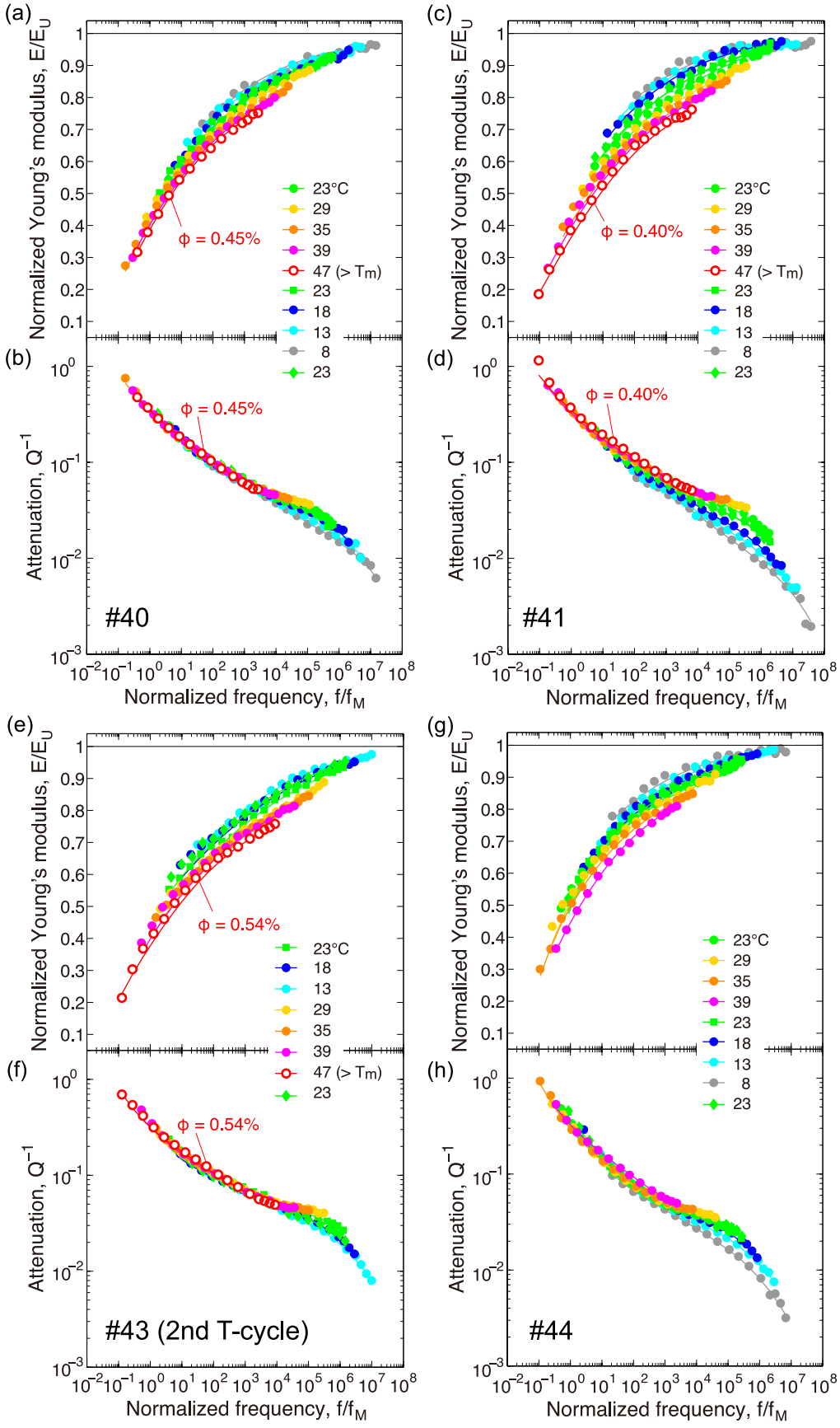

Figure 2.11: Young's modulus normalized to the unrelaxed modulus $E_U(T)$ and attenuation are shown for samples (a, b) #40, (c, d) #41, (e, f) #43 in the second temperature cycle, and (g, h) #44 as functions of the frequency normalized to the Maxwell frequency f/f_M. Explanations for color, symbol type, line, and order of legend are given in the caption of Figure 2.10.

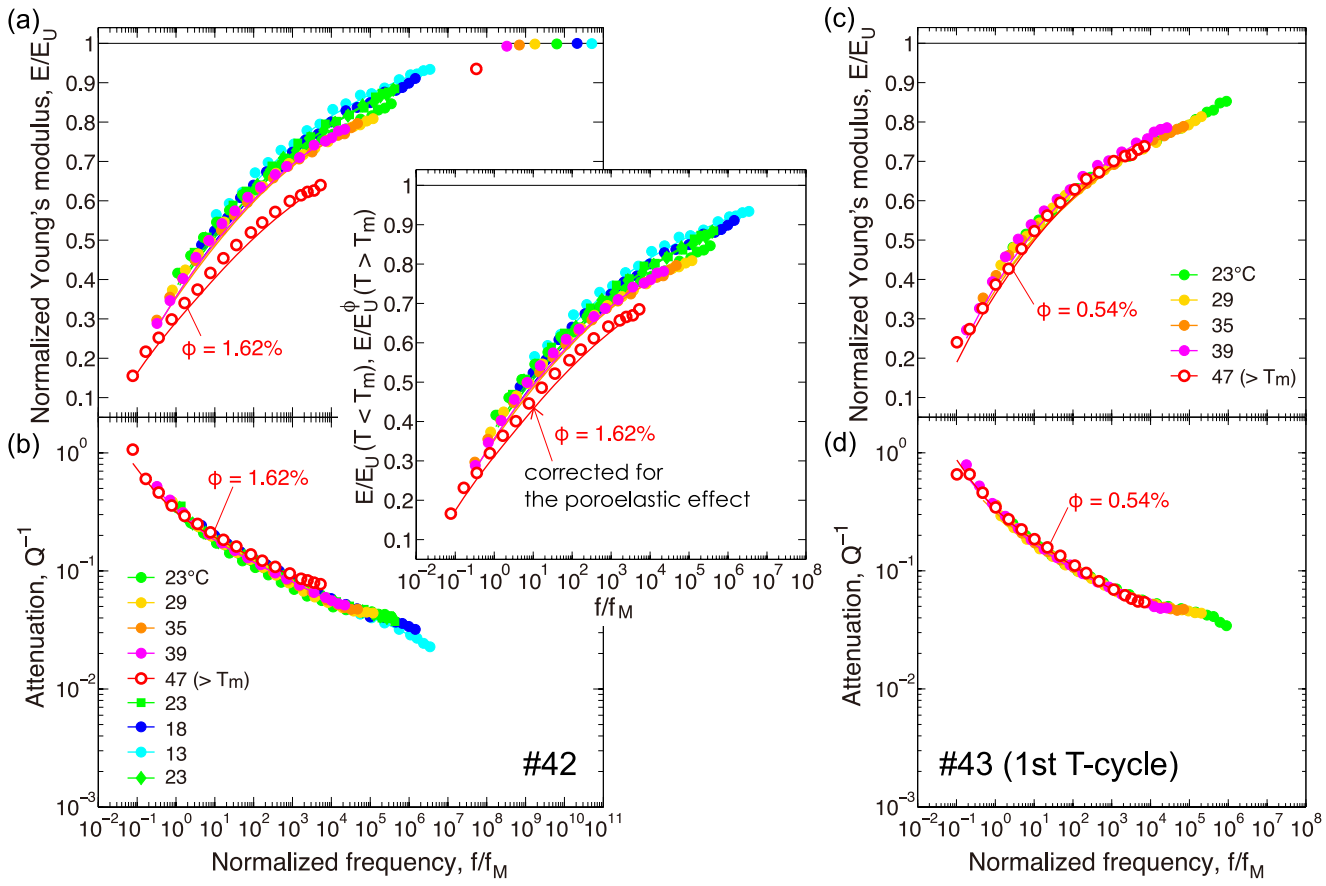

Figure 2.12: Young's modulus normalized to the unrelaxed modulus $E_U(T)$ and attenuation are shown for samples (a, b) #42 and (c, d) #43 in the first temperature cycle as functions of the frequency normalized to the Maxwell frequency $f/f_{\rm M}$. Also shown in Figure 2.12a are the ultrasonic data of this sample. In the inset of Figure 2.12a, E at 47°C is corrected for the poroelastic effect by normalizing E to E_U^ϕ obtained from the ultrasonic measurement of this sample at 47°C. Explanations for color, symbol type, line, and order of legend are given in the caption of Figure 2.10.

effect (Figure 2.7). When the E data in the partially molten state are corrected for the poroelastic effect by normalizing them to E_U^ϕ introduced in section 2.2.2 ($E_U^\phi/E_U = 0.935$ for sample #42), the discontinuity is mostly removed, but slightly remains (open symbols in the inset in Figure 2.12a). The discontinuity cannot be removed even by using the drained modulus, which is only 0.022 smaller than E_U^ϕ/E_U at $\phi = 1.6\%$. Therefore, when melt fraction is large ($> 1\%$), anelasticity may show a discontinuous change at the onset of melting.

2.2.5 Relaxation Spectrum X

The anelasticity data shown by E and Q^{-1} are further represented by using the relaxation spectrum X. Complex compliance ($J^* = J_1 + iJ_2$) of a linear viscoelastic material is generally represented by the unrelaxed compliance J_U ($= 1/E_U$), relaxation spectrum

$X(\tau)$, and viscosity η as

$$\begin{cases} J_1(\omega) = J_U \left[1 + \displaystyle\int_{\tau=0}^{\infty} X(\tau) \frac{1}{1+(\omega\tau)^2} \frac{\mathrm{d}\tau}{\tau} \right] \\ J_2(\omega) = J_U \displaystyle\int_{\tau=0}^{\infty} X(\tau) \frac{\omega\tau}{1+(\omega\tau)^2} \frac{\mathrm{d}\tau}{\tau} + \frac{1}{\omega\eta}, \end{cases} \tag{2.6}$$

where ω ($= 2\pi f$) and τ represent angular frequency and relaxation time scale, respectively [*Nowick and Berry,* 1972]. To confirm the linearity of the data, we measured E and Q^{-1} as functions of stress/strain amplitude at the supersolidus temperature. As shown in Figure 2.13, the dependence of E and Q^{-1} on the strain amplitude was small for the partially molten sample with the largest ϕ ($= 1.6\%$). The linearity of the melt-free samples was already shown by *Takei et al.* [2014]. These results show the validity of the analysis by using equation (2.6). Detailed procedures to estimate $X(\tau)$ from J_1 and J_2, or from E and Q^{-1}, are presented by *Takei et al.* [2014] and are not repeated here.

The obtained $X(\tau)$ is shown in Figure 2.14 as a function of time scale τ normalized to the Maxwell relaxation time $\tau_M = f_M^{-1}$. The validity of these results can be confirmed in Figures 2.10–2.12 (and A.1) by the good agreement between the symbols (measured) and lines (calculated from X). The relaxation spectra X plotted in Figures 2.14a–2.14d collapse onto a nearly single curve at $\tau/\tau_M \geq 2 \times 10^{-5}$, but does not at $\tau/\tau_M < 2 \times 10^{-5}$, similar to the Q^{-1} spectra shown in Figure 2.11. In contrast, the relaxation spectra X shown in Figures 2.14e and 2.14f collapse onto a single master curve for all τ/τ_M, similar

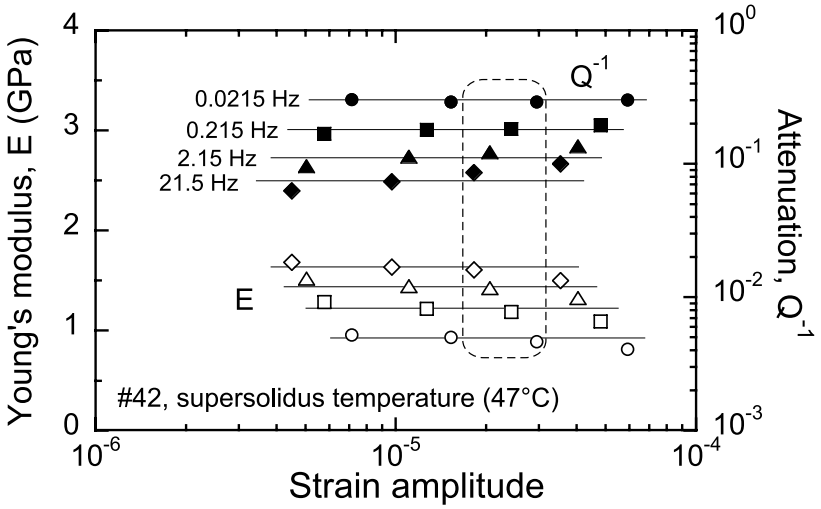

Figure 2.13: Young's modulus (open symbols) and attenuation (solid symbols) versus strain amplitude obtained by a partially molten sample. Symbol shape denotes a testing frequency (21.5 Hz (diamond), 2.15 Hz (triangle), 0.215 Hz (square), and 0.0215 Hz (circle)). The data encircled with a dashed line were obtained at the condition of this study.

to the Q^{-1} spectra of these samples shown in Figure 2.12.

Following *Takei et al.* [2014], the obtained relaxation spectra are represented by a superposition of a background dissipation and a high-frequency peak:

$$X(\tau) = X_B(\tau) + X_P(\tau). \tag{2.7}$$

The background dissipation is a monotonic spectrum defined as a function of normalized time scale $\tau_n = \tau/\tau_M$,

$$X_B(\tau_n) = A_B \times (\tau_n)^{\alpha}, \tag{2.8}$$

where the amplitude A_B and slope α are constants. The background dissipation follows the Maxwell frequency scaling. The high-frequency peak is defined by the deviation of X from the background X_B. It has a shape of broad peak, which can be roughly represented by a Gaussian distribution with the amplitude A_P, peak time scale τ_P, and peak width σ_P estimated by the least squares fitting [*Takei et al.*, 2014]. *Takei et al.* [2014] reported that the peak time scale τ_P/τ_M is a constant nearly independent of each experimental condition, but that the peak amplitude A_P and width σ_P increase with increasing T, d, and C. They showed that the variations of A_P and σ_P cause the breakdown of the Maxwell frequency scaling at the high normalized frequencies ($>\sim 10^4$), where X_P dominates over X_B. Therefore, in this study, by introducing the normalized peak time scale $\tau_n^P = \tau_P/\tau_M$, the high-frequency peak is expressed as

$$X_P(\tau_n, T/T_m, d, \phi) = A_P \exp\left(-\frac{\left(\ln(\tau_n/\tau_n^P)\right)^2}{2\sigma_P^2}\right), \tag{2.9}$$

where the total relaxation strength of the peak Δ_P is related to A_P and σ_P as $\Delta_P = \sqrt{2\pi}\sigma_P A_P$.

The background dissipation X_B obtained for each sample is shown by the black line in Figure 2.14. The parameter values are explicitly written as $A_B = 0.664$ and $\alpha = 0.38$ for #40, 41, and 43, $A_B = 0.716$ and $\alpha = 0.34$ for #42, and $A_B = 0.444$ and $\alpha = 0.38$ for #44. Although A_B and α for the subsolidus cycle (#44) are equal to those of *Takei et al.* [2014], A_B obtained for the supersolidus cycles were slightly larger.

Typical examples of the high-frequency peak X_P are shown in Figure 2.15 for samples #41 (without hysteresis) and #42 (with hysteresis). The data at $T \leq 23$°C have enough data points on both sides of the peak and hence reliable values for σ_P, A_P, and τ_n^P can be obtained by the fitting [*Takei et al.*, 2014]. The obtained parameters are shown in Figure

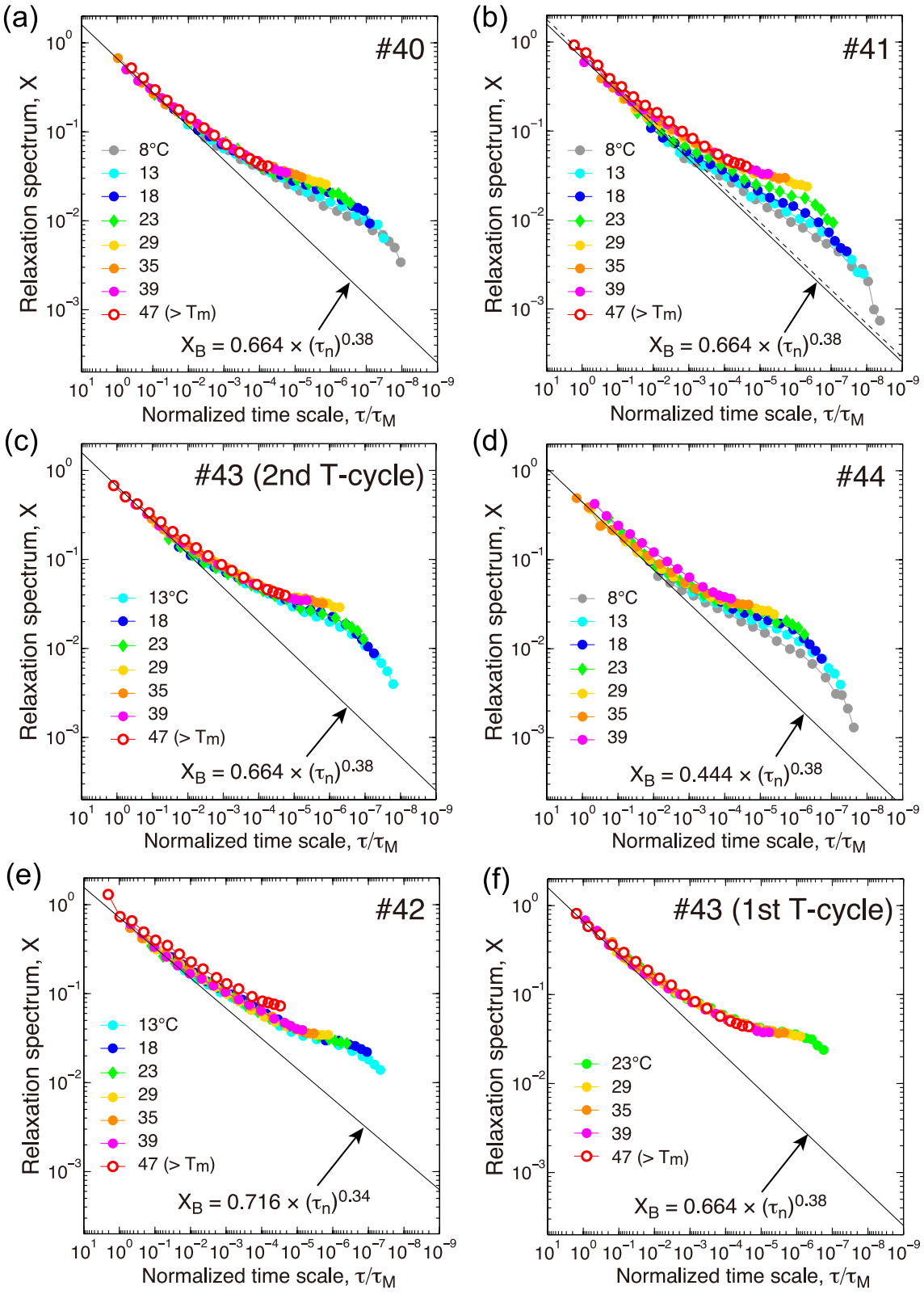

Figure 2.14: Relaxation spectrum X as a function of the time scale normalized to the Maxwell relaxation time τ/τ_M $(= \tau_n)$. (a) Sample #40, (b) #41, (c) #43 in the 2nd temperature cycle, (d) #44, (e) #42, and (f) #43 in the 1st temperature cycle. Legend is arranged in the order of temperature, where the same runs as those in Figures 2.10–2.12 are plotted by the same color and symbol type. Black solid line shows the background dissipation X_B. Dashed line in Figure 2.14b shows a possible uncertainty in X_B $(A_B = 0.75)$.

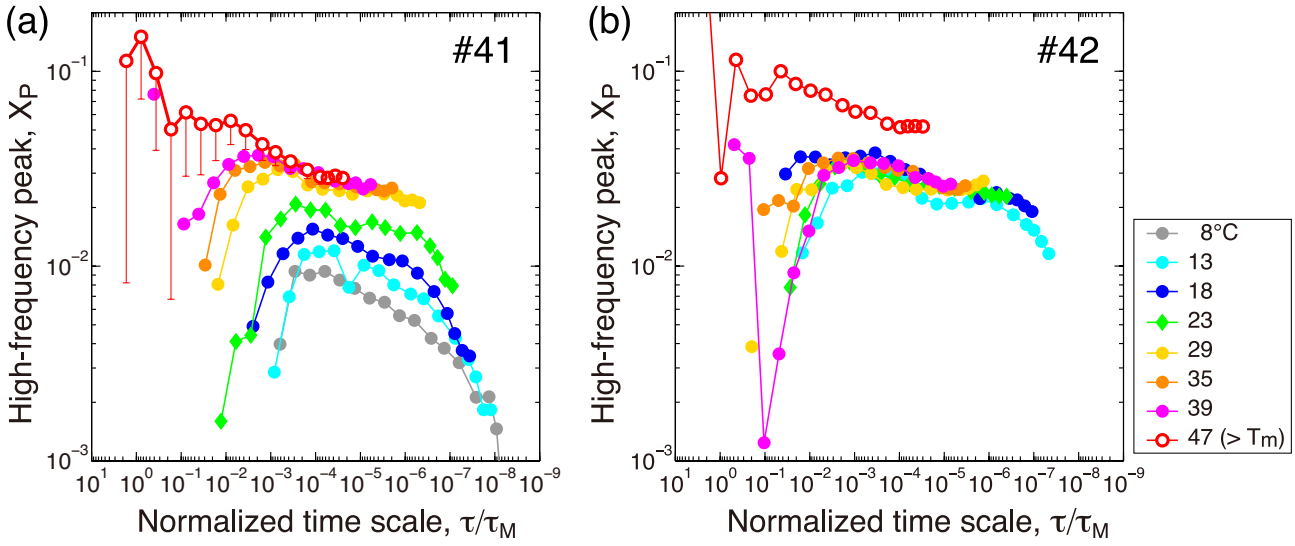

Figure 2.15: Typical examples of high-frequency peak X_P for samples (a) #41 (without hysteresis) and (b) #42 (with hysteresis), obtained by subtracting X_B from X in Figures 2.14b and 2.14e, respectively. The error bar in Figure 2.15a shows a possible uncertainty in X_P caused by that in X_B shown in Figure 2.14b (dashed line).

2.16 as a function of T/T_m (black symbols). These data show that $\tau_n^P (= 6 \times 10^{-5})$ is independent of each experimental condition and that A_P and σ_P increase with increasing T/T_m. These observations are consistent with the results of *Takei et al.* [2014]. At $T \geq 29$°C, the data points exist only on the longer time scale side of the peak and it is difficult to estimate σ_P and τ_n^P from the data fitting. For these data, as shown below, Δ_P was estimated by using the modulus data.

The total relaxation strength that exists above f, or below $\tau = (2\pi f)^{-1}$, is defined by

$$\Delta(f) = \int_{\tau=0}^{\infty} X(\tau) \frac{1}{1+(2\pi f\tau)^2} \frac{\mathrm{d}\tau}{\tau} = \frac{J_1(f) - J_U}{J_U} \tag{2.10}$$

[*Takei et al.*, 2014]. Even if X at small τ cannot be directly measured, the integral $\Delta(f)$ can be calculated by using the accurately measured $J_1(f)$. We calculated Δ_P from $\Delta(f_P)$ by using equation (B1) of *Takei et al.* [2014] with fixed $\tau_n^P = (2\pi f_P/f_M)^{-1} = 6 \times 10^{-5}$. (We used $\Delta_\infty = 0.015$ for #44 and 0.031 for the others. When $T > T_m$, $\Delta(f_P)$ was further corrected for the poroelastic effect by using the theoretical prediction in Figure 2.7.) Then, by estimating A_P as $A_P = X(\tau_P)$, σ_P was calculated from Δ_P and A_P. These results obtained from the modulus data are shown in Figure 2.16 by gray symbols. In Appendix B, the Gaussian distributions thus determined are plotted along with the X_P data for sample #41.

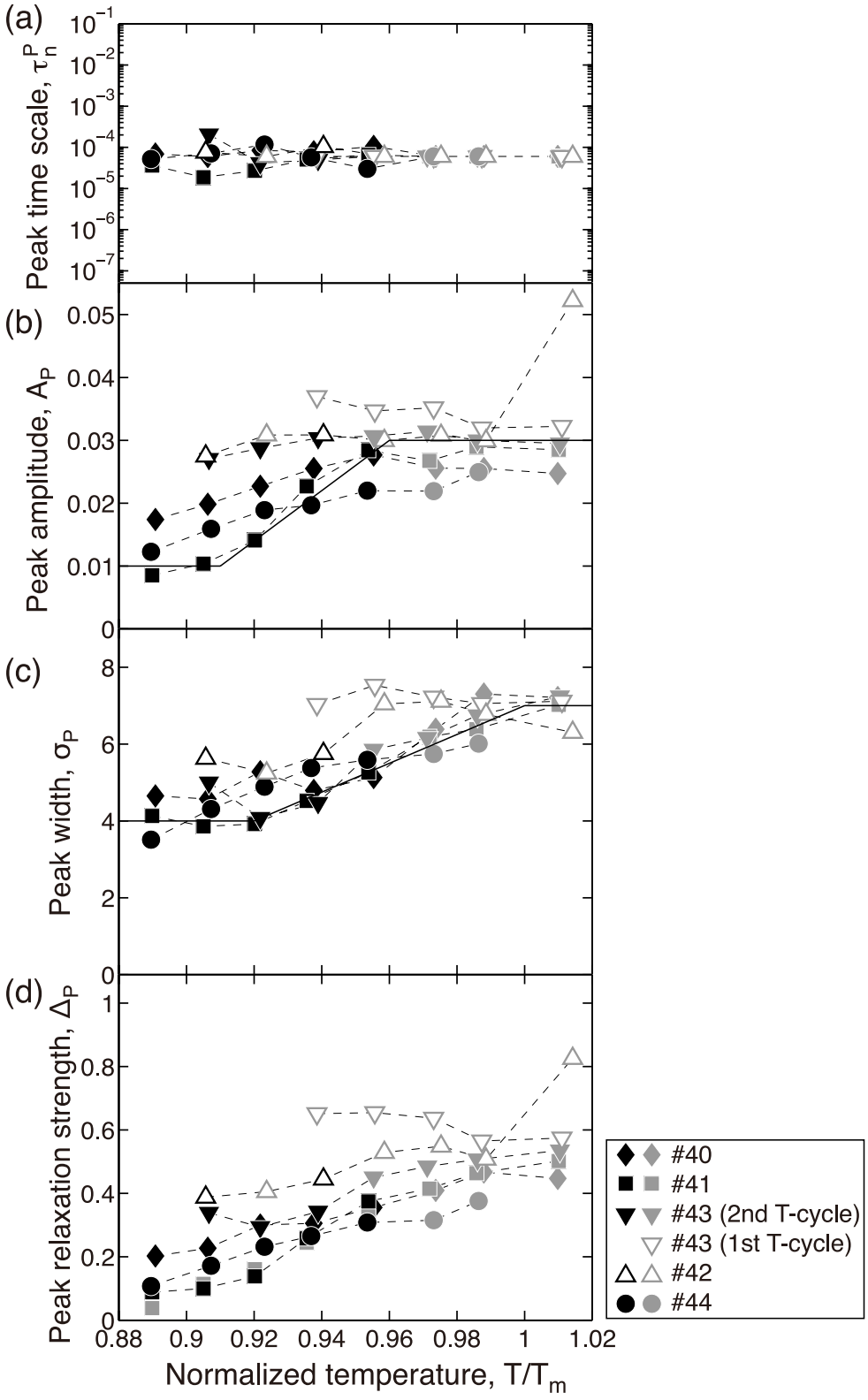

Figure 2.16: (a) Normalized peak time scale τ_n^P, (b) peak amplitude A_P, (c) peak width σ_P, and (d) total relaxation strength Δ_P of the high-frequency peak X_P are plotted as functions of normalized temperature T/T_m. Symbol shape shows each sample. Black symbols show the parameters obtained by the fitting to X_P, and gray symbols show those obtained by using the modulus data. Each data point at $T/T_m = 0.94$ shows the average of several measurements during the cycle. Solid line in Figure 2.16b shows empirical formula (3.3), and that in Figure 2.16c shows (3.4).

2.2.6 Elasticity, Anelasticity, and Viscosity at Near-solidus Temperatures

Temperature dependences of elasticity, anelasticity, and viscosity near $T = T_m$ are summarized in Figure 2.17. The bottom panel shows the total relaxation strength above $f/f_M = 10^3$, $\Delta(f/f_M = 10^3)$, which is calculated from J_1 by using equation (2.10). The horizontal line labeled "background" shows $\Delta(f/f_M = 10^3)$ calculated from X_B, which is constant because X_B follows the Maxwell frequency scaling. The deviation of $\Delta(f/f_M = 10^3)$ from this horizontal line shows the relaxation strength associated with the high-frequency peak X_P; the deviation increases with increasing T/T_m, showing the breakdown of the Maxwell frequency scaling. Without the hysteresis, $\Delta(f/f_M = 10^3)$ significantly increases at near-solidus temperatures (black solid and gray symbols). Although this trend was already reported by *Takei et al.* [2014] at $T/T_m \leq 0.93$ (gray symbols in Figure 2.17), we have confirmed that it does continue up to $T/T_m > 1$. We also captured some discontinuous increase in anelasticity at $T/T_m = 1$ for #42 with $\phi = 1.6\%$, but it was negligibly small for $\phi < 1\%$ (red symbols). Once the sample is partially molten, $\Delta(f/f_M = 10^3)$ sometimes remains at a high level even below the solidus temperature and becomes insensitive to temperature (open symbols). With this hysteresis, the peak dissipation follows the Maxwell frequency scaling. Also shown in Figure 2.17 are typical behaviors of elasticity and viscosity (top and middle panels). The enhanced reduction of viscosity with a higher activation energy (middle panel) and the significant increase in anelasticity (bottom panel) occur almost simultaneously, but the reduction of the ultrasonic wave velocity occurs much more steeply than these (top panel).

2.3 Discussion

In this study, elasticity, anelasticity and viscosity of polycrystalline aggregates were measured at the near-solidus temperatures to investigate the effect of partial melting. Generally, clear definitions of the solidus temperature and partial melting are difficult, because of a possible existence of a very small amount of melt generated below the solidus by impurities [e.g., *McKenzie*, 1985; *Hirschmann*, 2010]. However, in this study, we can define the solidus temperature by $T_m = 316$ K (43°C) and can define the partial melting as follows. The samples used in this study and in *Takei et al.* [2014] have two types of microstructure. Sample #44 and the binary samples of *Takei et al.* [2014], which were pre-annealed just below the solidus temperature (40°C and $T/T_m = 0.991$), have dispersed

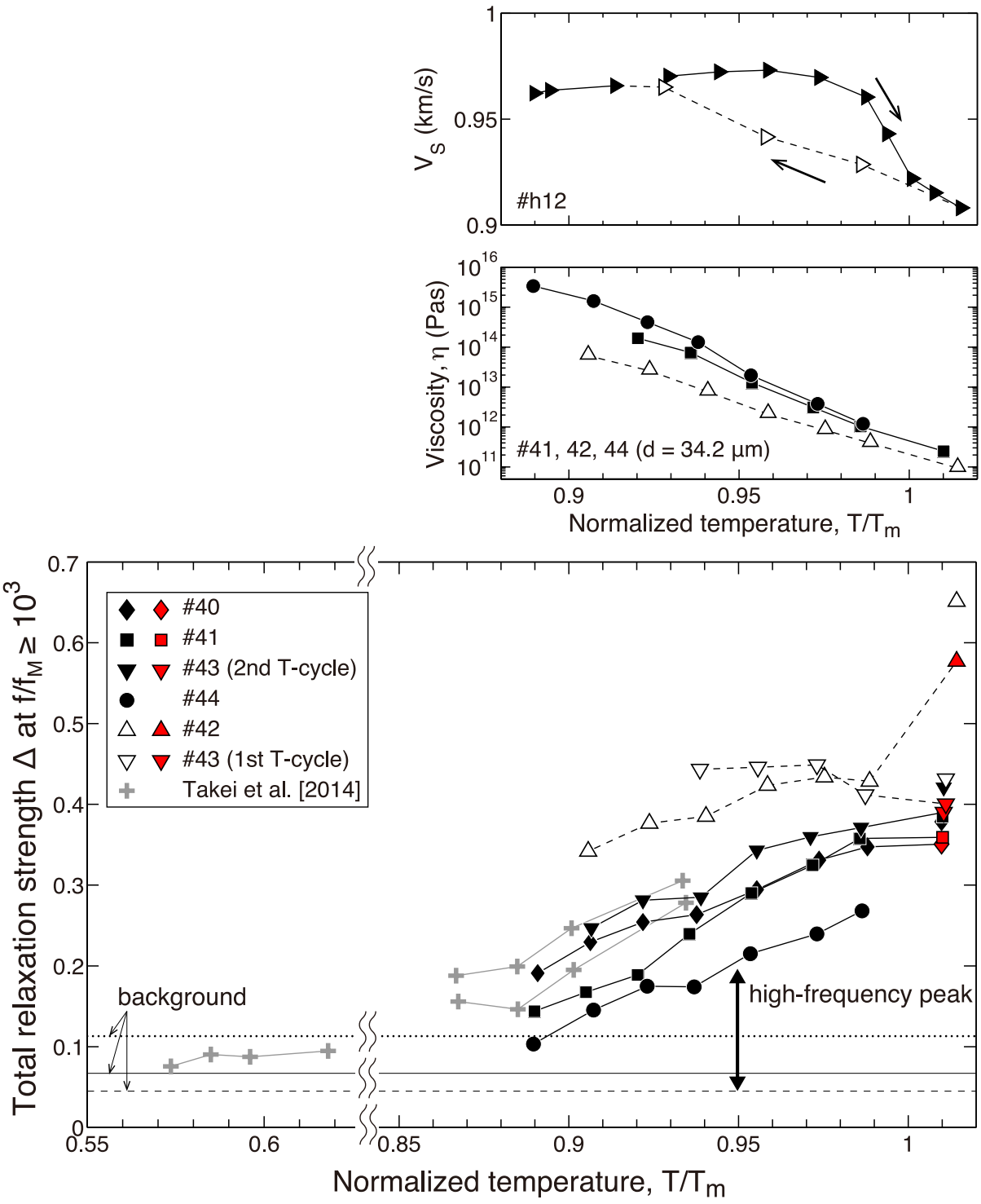

Figure 2.17: (top) Elasticity, (middle) viscosity, and (bottom) anelasticity versus normalized temperature T/T_m, where T_m represents solidus or melting temperature of each sample. Black symbols show the present data, where symbol shape shows each sample. Gray cross symbols show our previous data (37BD2L, 34BD1L, and 27pureS in *Takei et al.* [2014]). The bottom panel plots the total relaxation strength Δ at $f/f_M \geq 10^3$ calculated by equation (2.10), where the horizontal lines show Δ at $f/f_M \geq 10^3$ calculated from the background dissipation X_B (solid: #40, 41, 43, dashed: #44, dotted: #42). The difference from this line is caused by the high-frequency peak X_P. At $T > T_m$, both before and after the correction for the poroelastic effect are shown by black and red symbols, respectively. Each data point at $T/T_m = 0.94$ shows the average of several measurements during the cycle. In all plots, open symbols show the data strongly influenced by the hysteresis of partial melting.

diphenylamine grains (Figure 2.3b). Samples #40–43, which were pre-annealed just above the solidus temperature (47°C and $T/T_m = 1.013$ for #40, 47–55°C and $T/T_m = 1.013$–1.038 for #41–43), have connected network of the grain-edge tubules (Figures 2.3c and 2.3d), which were filled with solidified melt during the microstructural observation at the room temperature. Therefore, partial melting can be clearly defined in the present binary system as a formation of the tubule network at $T/T_m = 1.00 \pm 0.01$. High-temperature annealing below $T/T_m = 0.991$ does not leave any sign of melting in the microstructure. In other words, the variations of the mechanical properties at $T/T_m < 0.991$ occur in the absence of the melt phase, whereas those at $T/T_m \geq 1.00$ occur in the presence of the melt phase with the melt fractions of 0.4–1.6%. In this section, the variations of the viscoelastic properties with temperature and/or samples obtained in this study and in *Takei et al.* [2014] are discussed in detail based on the understanding of T_m mentioned above.

2.3.1 Ultrasonic Data

As shown by Figure 2.7, the reduction of the ultrasonic velocities at $T \geq T_m$ can be explained quantitatively by the poroelastic effect predicted for the present samples with dihedral angle $\theta = 34.6°$. Although this requires that the melt squirt flow, which completes the poroelastic effect by relaxing the liquid pressure heterogeneity between the neighboring pores [*Mavko and Nur*, 1975], has a higher characteristic frequency f_{squirt} than the ultrasonic frequency (700 kHz), the estimation of f_{squirt} = a few MHz for the present samples [*Takei*, 2000] satisfies this requirement. An important consequence of this result is that the large high-frequency peak captured by the forced oscillation test under the partially molten condition is caused by some other mechanism than the melt squirt flow. The ultrasonic velocity starts reducing at $T/T_m = 0.975(< 0.99)$ and hence starts reducing in the absence of melt (Figures 2.5 and 2.17). Although this process cannot be explained by the poroelastic effect, because the final velocity reductions at $T \geq T_m$ can be explained well by the elastic effect of the melt phase, the slight reduction at $T/T_m < 0.99$ should be considered as the initiation of the poroelastic effect.

2.3.2 Anelasticity and Viscosity

2.3.2.1 Changes below the Solidus Temperature: Premelting?

The most remarkable observation of this study and of *Takei et al.* [2014] is that the amplitude and width of the high-frequency peak X_P start growing from considerably below the solidus temperature (Figures 2.16–2.17). This observation indicates that a solid-state mechanism is active in the high-frequency peak X_P. The total relaxation strength of the poroelastic effect Δ_{poro} under the undrained or drained condition is almost proportional to melt fraction ϕ and hence small for a small ϕ (Figure 2.18). In contrast, the total relaxation strength of the high-frequency peak Δ_P at $T \geq T_m$ is more than one order of magnitude larger than Δ_{poro} and remains to be large even at a small ϕ ($< 1\%$) (Figure 2.18). The small amplitude of the poroelastic effect cannot explain the large Δ_P particularly at very small ϕ, and we have to introduce some other mechanism than the poroelastic effect to explain the high-frequency peak X_P. This conclusion is also supported by the ultrasonic data discussed in section 2.3.1. Because a solid-state mechanism is required, and because the peak time scale τ_P is closely related to the Maxwell relaxation time scale τ_M, the most plausible mechanism of X_P is the diffusionally accommodated grain boundary sliding, which is equal to the mechanism of the background dissipation X_B. The possibility of elastically accommodated grain boundary sliding [*Raj and Ashby*, 1971] is not supported by the independence of τ_P/τ_M from grain size [*Takei et al*, 2014]. Although mutual relationship of the grain boundary sliding to the partial melting has not been known so far, the present data indicate that the dynamical property of the grain boundary changes near the solidus temperature and significantly changes the shape of the relaxation spectrum at short normalized time scales. The mechanical properties in the partially molten state are affected both by this change in the grain boundary and by the change directly caused by the melt phase, such as the poroelastic effect. As a result, the effects of the partial melting on the mechanical properties are significantly larger than those estimated by the poroelastic effect alone. In particular, Δ_P dominates over Δ_{poro} at very small ϕ.

The interpretation that the temperature dependence of Δ_P is caused by a change in the dynamical property of the grain boundary just below the solidus temperature is only a hypothesis. However, structural transition of grain boundary below the bulk melting point has been known as "premelting" [e.g., Wolf, 2001]. If a similar structural change

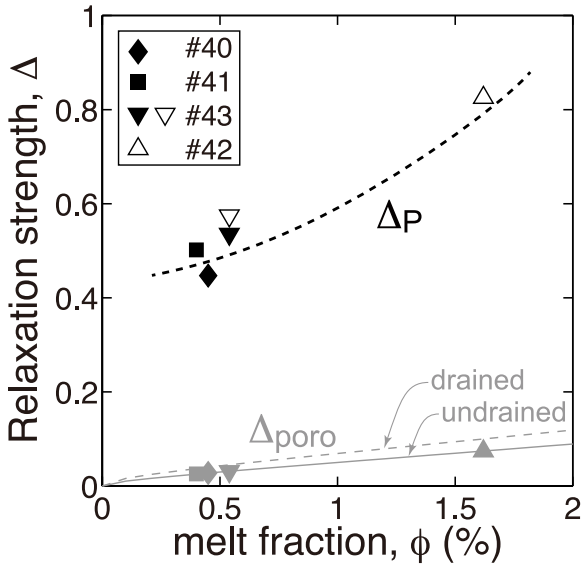

Figure 2.18: Total relaxation strength of high-frequency peak Δ_P at $T > T_m$ (black) and that of poroelastic effect $\Delta_{\rm poro}$ (gray) are plotted as functions of melt fraction ϕ. $\Delta_{\rm poro}$ is shown for both undrained and drained conditions.

occurs below the solidus temperature, it explains well the growth of Δ_P and also the large amplitude of Δ_P even for a small ϕ. Effect of partial melting has been considered mostly within the framework of the direct effect which is caused by the presence of the melt phase. However, this hypothesis proposes another possibility beyond this framework. Similar hypothesis was once introduced by *Priestley and McKenzie* [2006] to explain the seismic velocity data, but further examination of this hypothesis has not been performed. If such process is active in the Earth, it significantly influences the interpretation of the seismic low velocity regions in the upper mantle. We consider it important to further test this hypothesis by experimental and theoretical studies.

In this study, we also captured the steeper reduction of viscosity represented by the higher activation energy at $T \geq 23$°C ($T/T_m \geq 0.937$), which was not recognized in the previous experiments conducted at lower run temperatures than 23°C [*Takei et al.* 2014]. As shown by the difference between the asterisk and cross symbols in Figure 2.9c, the extra reduction due to the increase in the activation energy is a factor of 5 at $T \geq T_m$, which is not sensitive to the concentration of the secondary component. This extra reduction of viscosity and the growth of Δ_P are roughly simultaneous (Figure 2.17). We consider that the extra reduction of viscosity is also resulted from the change in the dynamical property of the grain boundary. As a result, the viscosity in the partially molten state is influenced both by this change in the grain boundary (probably) and by the change

directly caused by the melt phase.

In this subsection, we discussed the behavior at $T < T_m$ observed commonly in both subsolidus and supersolidus cycles (Figure 2.1b). In the next subsection, we discuss the hysteresis, which was observed in the supersolidus cycle, but not in the subsolidus cycle.

2.3.2.2 Insights from the Hysteresis

The hysteresis effect was captured as the enhanced anelastic relaxation (that is, large and broad X_P) and enhanced viscous deformability at $T < T_m$ (e.g., open symbols in Figures 2.9 and 2.16). This effect is newly recognized in this study. Because the hysteresis did not occur in the subsolidus cycle performed on sample #44 and in *Takei et al.* [2014], the hysteresis is considered to be caused by the existence of the tubule network which is filled with small crystals solidified from the melt phase. The observed hysteresis can be understood by considering that the solidified melt has higher diffusivity than the surrounding matrix and the matter diffusion is enhanced by the presence of this network. With this hypothesis, the strongest hysteresis of sample #42 ($\phi = 1.6\%$, $d = 46.3$ μm) and the 2nd strongest hysteresis of #43 ($\phi = 0.54\%$, $d = 39.7$ μm) can be explained well by the large melt fraction and/or large grain size of these samples, because the tubules are thinner for smaller melt fraction and/or smaller grain size, and are expected to be difficult to keep the full connectivity during the crystal growth in the tubules at $T < T_m$. This expectation is supported by the observation that when $\phi = 1.6\%$, melt pockets are found at almost all triple junctions (Figure 2.3c), but when $\phi < 1\%$, melt pockets are absent from a large number of triple junctions (Figure 2.3d). The isolated melt pockets sometimes observed along the grain boundaries (white arrows in Figures 2.3c and 2.3d) are considered to be an indication of the disconnection by necking. Under the strong hysteresis, X_P fully follows the Maxwell frequency scaling (Figure 2.12), suggesting that the active mechanism is the diffusionally accommodated grain boundary sliding. This gives another support to the hypothesis that X_P is caused by this mechanism and not by the elastically accommodated grain boundary sliding, providing an important clue to develop a theoretical model of X_P.

The occurrence of the hysteresis suggests that the matter diffusivity is enhanced by the network of solidified melt. Therefore, when we look at the results of the supersolidus cycles, we have to take into account the following consequences of the network. One of our major concerns in this study is whether or not the formation of the connected

melt network at $T = T_m$ discontinuously increases the matter diffusivity, which causes a discontinuous change in the mechanical properties [*Takei and Holtzman*, 2009a, 2009b]. However, such discontinuity can be smeared and smoothed by the fast diffusion path at $T < T_m$. In this sense, the supersolidus cycle performed in this study may not be the best way to examine the existence or nonexistence of the mechanical discontinuity. Although a sample prepared by the subsolidus annealing is suitable for this examination, such sample causes a rapid grain growth at the onset of melting, which results in the growth of pores at ambient pressure. The present data from the supersolidus cycle are important to investigate the effects of partial melting without the effects of grain growth nor void growth. Therefore, in section 2.3.2.3, by keeping the limitation mentioned here in mind, we discuss the existence and nonexistence of discontinuity by using the present data. The possibility of the smoothing also means that even if a gradual change below the solidus temperature is captured in the supersolidus cycle, it is difficult to distinguish between smoothed discontinuity and premelting. In order to avoid this ambiguity, the subsolidus cycle was performed on the sample #44 with dispersed diphenylamine grains. All the changes discussed in section 2.3.2.1 did occur in all subsolidus cycles in this study and in *Takei et al.* [2014], as well as in the supersolidus cycles without the strong hysteresis, and hence do not depend on the microstructure.

2.3.2.3 Direct Effect of Melt

Although the direct effects of the melt phase on elasticity and viscosity have been studied intensively, that on anelasticity is poorly understood. As we discussed in section 2.3.1, the poroelastic effect consistent with the theoretical prediction was obtained by the ultrasonic data. This effect was removed from the modulus data in the partially molten state measured by the forced oscillation test, so that the total relaxation strength of the high-frequency peak Δ_P at $T > T_m$ does not include the poroelastic effect. A discontinuous increase of Δ_P at $T = T_m$ was observed for the largest melt fraction sample (#42 with $\phi = 1.6\%$), but not for the other samples with $\phi < 1\%$ (Figures 2.16d and 2.17 bottom). Therefore, the present data show that when melt fraction is not so small, Δ_P is increased discontinuously by the presence of the melt phase. This change breaks the Maxwell frequency scaling. In addition to such direct effect of melt on Δ_P, if the anelastic effect is evaluated at a given frequency f (Hz), it is affected by the direct effect of melt on viscosity, because viscosity affects the Maxwell frequency f_M used to normalize f. This direct effect

of melt on anelasticity through the effect on f_M is treated within the framework of the Maxwell frequency scaling.

Theoretical studies have shown that the melt phase significantly enhances the grain boundary diffusion creep because of its small viscosity and high diffusivity [*Cooper et al.,* 1989; *Takei and Holtzman*, 2009a, 2009b]. The direct effect of the melt phase consistent with the theoretical prediction was captured by the exponential dependence of viscosity on ϕ shown in Figure 2.9c. The model by *Takei and Holtzman* [2009a, 2009b] further predicted that when melt forms a connected network at $T = T_m$, viscosity decreases discontinuously by a factor of 5. However, in this study, the discontinuity clearly attributable to the formation of a connected network was not captured. The discontinuous reduction of viscosity is particularly expected for sample #44 with dispersed diphenylamine grains. Because this sample was not tested above the solidus temperature, we use the supersolidus data of #42 with a similar chemical composition to #44 instead. Although the two samples are different in grain size, this effect on viscosity is known (Figure 2.9a). In the viscosity plot corrected for the grain size effect (Figures 2.9b and 2.17 middle), the data point of sample #42 ($\phi = 1.6\% \simeq 2\%$) in the partially molten state with a connected melt network lies on the smooth extension of the data of #44 with dispersed diphenylamine grains, showing no discontinuity. Even for a sample with solidified melt tubules, if the network is disconnected at $T < T_m$, the reconnection of the network at $T = T_m$ is expected to cause a mechanical discontinuity. However, the samples used in the supersolidus cycle did not show any viscosity jump at $T = T_m$, either (Figures 2.9b). Therefore, the present data do not support the theoretical prediction by *Takei and Holtzman* [2009a, 2009b].

When melt fraction is small ($< 1\%$), the direct effects of melt on Δ_P and on viscosity were both very small and hence cause no discontinuous change in anelasticity and viscosity at $T = T_m$. In the applications in Chapters 3–4, by following the present results, we do not include any discontinuous change at $T = T_m$ to analyse the seismic data of a region where melt fraction is considered to be not so large. However, as discussed in section 2.3.2.2, it is desired to further check this conclusion by partially melting a sample with dispersed secondary phase. Also, the discrepancy from the theory by *Takei and Holtzman* [2009a, 2009b] has to be studied further.

2.3.3 Comparison with Other Studies

A large high-frequency peak similar to this study was observed in the attenuation spectra of the melt-bearing olivine aggregates [*Jackson et al.*, 2004]. As summarized in *Takei et al.* [2014], it shows a similarity to the peak observed by *Takei et al.* [2014], and hence we consider that the underlying mechanism of the peak has something in common between these two polycrystalline materials. However, the mechanism of the peak proposed by *Jackson* [2015] and *Faul and Jackson* [2015] is the melt squirt flow, which is quite different from the present conclusion that the high-frequency peak is caused by a solid-state mechanism. One reason for this disagreement is that, as discussed in section 2.3.2, the existence of the peak below the solidus temperature plays an important role in our estimation of the mechanism, but the data below the solidus temperature were not used in their study, probably because of the difficulty to accurately determine the solidus temperature in their study. Another reason for the disagreement is that the melt geometry considered in the two studies is quite different. Here, we discuss this latter point in some detail.

The total relaxation strength of the poroelastic effect Δ_{poro} and characteristic frequency of the melt squirt flow f_{squirt} depend on the melt geometry. The equilibrium melt geometry is similar between the present samples (dihedral angle $\theta = 34.6°$) and the olivine-basalt system ($20° \leq \theta \leq 40°$, *Holness* [1997]). In order to obtain large Δ_{poro} and small f_{squirt} comparable to Δ_P and f_P, respectively, melt geometry must be largely different from the equilibrium geometry. *Jackson* [2015] and *Faul and Jackson* [2015] considered thin melt films, based on the observation of *Garapić et al.* [2013]. However, it is difficult to apply the film geometry to the present samples for the following three reasons. First, in the present organic samples, invisibly thin melt films, if any, are expected to be visible by preferential sublimation at the melt-grain interface. However, the microscopic observation of the cross sections shows that most of the melt pockets exist at triple junctions rather than along grain boundaries (Figures 2.3c and 2.3d). Second, the agreement between the poroelastic effect calculated by assuming the equilibrium melt geometry and the ultrasonic results can be obtained robustly for various ϕ and θ (section 2.2.2 and *Takei* [2000]), indicating that the assumed geometry is correct. Third, the steady-state viscosity of grain boundary diffusion creep is much more sensitive to the melt geometry than the elastic property [*Takei and Holtzman*, 2009a]. As a result, if $\Delta_{\mathrm{poro}} = 0.5$, the steady-state viscosity must be about 40 times smaller than that without melt, which is not consistent with the present

viscosity data (Figure 2.9c). Therefore, even if the data below the solidus temperature were not taken into account, the high-frequency peak in this study cannot be attributed to the melt squirt flow mechanism.

McCarthy and Takei [2011] reported that their data are consistent with the theoretical prediction by *Takei and Holtzman* [2009a] that the partial melting discontinuously reduces the diffusion creep viscosity by a factor of 5. However, the present data obtained by using the same material did not show a discontinuity in viscosity. We note that this apparent disagreement does not mean any inconsistency between the two data sets. We measured viscosity from $T = 0.89T_m$ to $1.01T_m$ as a nearly continuous function of T, but the measurement by *McCarthy and Takei* [2011] was only at $T = 0.94T_m$ and $1.02T_m$. In this study, as discussed in section 2.3.2.1, the extra reduction of viscosity occurred not discontinuously at $T = T_m$, but gradually at $0.94T_m \leq T \leq T_m$ by increasing the activation energy in this temperature range. Therefore, if viscosity is measured only at $0.94T_m$ and $1.02T_m$, the gradual change cannot be distinguished from the discontinuous change at $T = T_m$. The careful measurement of this present study revealed that most of the extra change occurs below T_m, in the absence of melt, and hence cannot be attributed to the discontinuous change theoretically predicted by *Takei and Holtzman* [2009a] by assuming the existence of the melt phase. We further note here that although *McCarthy and Takei* [2011] analysed their data by assuming that chemical effect does not depend on temperature, *Takei et al.* [2014] showed that the activation energy is different between the high-purity samples and the binary samples and hence this assumption is not valid. However, it is difficult to reanalyses their data: their samples contained pores resulted from the grain growth at ambient pressure, and probably due to this difference, the measured viscosity and activation energy are different from those measured in this study and in *Takei et al.* [2014] on the pore-free samples.

Zimmerman and Kohlstedt [2004] reported the diffusion creep viscosity of lherzolite at near-solidus temperatures. Their data do not show a discontinuous change at the solidus temperature ($T_m = 1160°C$). In comparing our data to theirs, we should note the difference that melt fraction increases discontinuously at $T = T_m$ in the present binary system and gradually with temperature in their multicomponent system (Figure A2 in *Zimmerman and Kohlstedt* [2004]). However, the theory predicts that the critical melt fraction ϕ_c needed for the reduction is very small ($\phi_c << 1\%$, *Takei and Holtzman* [2009b];

Holtzman [2016]), and hence discontinuous reduction in viscosity is expected to occur within, at least, 20°C from T_m (= 1160°C). However, such a steep change in viscosity is not observed in their data. Therefore, the present data agree with their data about the absence of discontinuity. Because their data are limited to $T/T_m \geq 0.96$, it is difficult to discuss the possible change in activation energy below the solidus temperature.

Here, we note that when two data obtained below and above the solidus temperature are largely different, we usually consider that the difference is caused at the solidus temperature due to the onset of melting. However, the result of this study proposes another possibility that the large difference is caused just before the melting.

2.4 Summary of the Experimental Study

I found that the effect of "partial melting" on the mechanical properties occurs by two stages: first, just before melting and second, at the onset of partial melting. Just before partial melting ($0.92 \sim< T/T_m < 1$), amplitude and width of the high-frequency peak X_P significantly increase, and viscosity of the grain-boundary diffusion creep is reduced significantly. These mechanical changes in the solid state are considered to be caused by a change in the dynamic property of grain boundary by premelting. At the onset of melting ($T/T_m = 1$), further changes in elasticity, anelasticity, and viscosity occur due to the direct effect of melt. They are reduction of elasticity due to the poroelastic effect, increase of the amplitude of X_P, and reduction of viscosity by a factor of $e^{-\lambda\phi}$. The former subsolidus changes have large amplitudes even for the samples which generate very small melt fraction (ϕ = 0.4–0.54%) at $T = T_m$. In contrast, the latter changes at $T = T_m$ are negligibly small for a very small melt fraction. In the upper mantle, melt fraction is considered to be very small ($\ll 1\%$) based on the geochemical studies [e.g., *McKenzie*, 2000]. Therefore, the premelting effect plays an important role in the interpretations of the low-velocity and high-attenuation zones in the upper mantle.

Chapter 3

New Anelasticity Model and its Applicability to the Mantle

The experimental result in Chapter 2 shows that the large high-frequency peak X_P is caused by a solid-state mechanism (probably, by diffusionally accommodated grain boundary sliding) in the absence of the melt phase. The growth and broadening of X_P occur just below the solidus temperature. Seismic waves have high normalized frequencies and can be influenced only by the broadened relaxation spectrum. As a result, the anelastic effect on the seismic waves is closely related to the partial melting. Such a mutual relationship between anelasticity and partial melting has not been pointed out so far. *McCarthy et al.* [2011] proposed a master curve model by assuming a constant spectrum shape $X(\tau_n)$ independent of the normalized temperature T/T_m. However, as shown in sections 2.2.4–2.2.5, this assumption is not valid at high normalized frequencies and the spectrum shape depends on T/T_m. As an important consequence of this difference, the model of anelasticity proposed by this study predicts much steeper reduction of the seismic wave velocity at near-solidus temperatures than the master curve model. In this chapter, I present a new anelasticity model based on the present experimental results (section 3.1). Applicability of this model to the mantle is tested by using the tomographic model of the Pacific mantle obtained by *Priestley and McKenzie* [2013] (section 3.2). The new anelasticity model is also completed by this test, in which we can obtain several material parameters representing the elasticity and viscosity of the peridotite as fitting parameters [*Priestley and McKenzie*, 2013]. In the next chapter, I further apply the new anelasticity model obtained in this chapter to the seismic discontinuity at the lithosphere-asthenosphere boundary.

3.1 Parameterization

The relaxation spectrum of shear modulus μ is expressed as

$$X(\tau, T, d, P, \phi \text{ or } C) = X_B(\tau_n) + X_P(\tau_n, T_n) \tag{3.1}$$

with normalized time scale $\tau_n = \tau/\tau_M$ and normalized temperature $T_n = T/T_m$ (defined by T K and T_m = solidus temperature K). The background X_B and peak X_P are given by

$$\begin{cases} X_B(\tau_n) & = & A_B\,(\tau_n)^\alpha \\ X_P(\tau_n, T_n) & = & A_P \exp\left(-\dfrac{\left(\ln(\tau_n/\tau_n^P)\right)^2}{2\sigma_P^2}\right), \end{cases} \tag{3.2}$$

where amplitude A_B and slope α of X_B and normalized time scale τ_n^P of X_P are constants, and amplitude A_P and width σ_P of X_P are given as functions of T_n:

$$A_P(T_n) = \begin{cases} 0.01 & \text{at } T_n < 0.91 \\ 0.01 + 0.4(T_n - 0.91) & \text{at } 0.91 \le T_n < 0.96 \\ 0.03 & \text{at } 0.96 \le T_n < 1 \\ 0.03 + \beta(\phi) & \text{at } 1 \le T_n \end{cases} \tag{3.3}$$

$$\sigma_P(T_n) = \begin{cases} 4 & \text{at } T_n < 0.92 \\ 4 + 37.5(T_n - 0.92) & \text{at } 0.92 \le T_n < 1 \\ 7 & \text{at } 1 \le T_n. \end{cases} \tag{3.4}$$

The term $\beta(\phi)$ in (3.3) is introduced to represent the direct effect of the melt phase on Δ_P, which was nearly zero at very small ϕ. Good agreement between these empirical formulae and the data are shown in Figure 2.16. Figure 3.1 shows X versus τ/τ_M for $T/T_m = 1$ and ≤ 0.9, using the parameter values summarized in Table 3.1. Also shown in this figure is the master curve proposed by *McCarthy et al.* [2011]. The dependence of A_P and σ_P on T_n given by equations (3.3) and (3.4) causes the breakdown of the Maxwell frequency scaling. Although A_P and σ_P depend on the grain size in *Takei et al.* [2014], the dependence on d was not so clear in this study by using the larger grain size samples than theirs. We therefore consider that the the effects of d on A_P and σ_P are saturated and apply the present results of A_P and σ_P directly to the Earth.

Because X smoothly depends on τ_n, by substituting (3.1) and (3.2) into the approximate formulae given by equations (18) of *McCarthy et al.* [2011], complex compliance

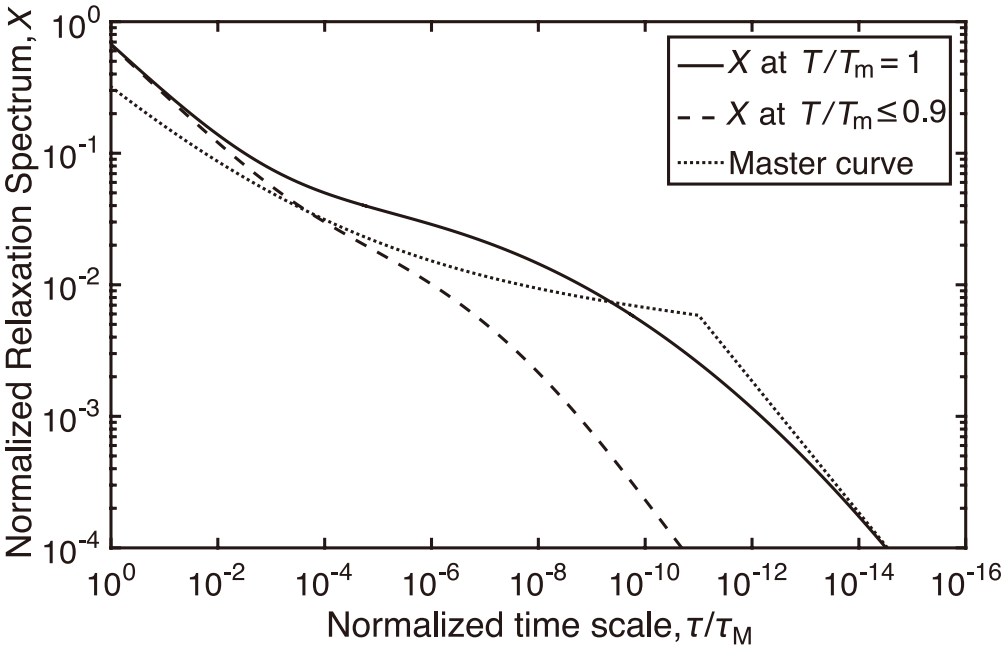

Figure 3.1: Normalized relaxation spectrum X of the new anelasticity model proposed in this study depends on the normalized temperature T/T_m. The spectra at $T/T_m = 1$ (solid line) and $T/T_m \leq 0.9$ (dashed line) are compared to the master curve proposed by *McCarthy et al.* [2011] (dotted line).

$J^* = J_1 + iJ_2$ can be obtained as

$$\left\{ \begin{array}{rcl} J_1(\tau_n^S) & = & J_U \left[1 + \dfrac{A_B(\tau_n^S)^\alpha}{\alpha} + \dfrac{\sqrt{2\pi}}{2} A_P \sigma_P \left\{ 1 - \mathrm{erf}\left(\dfrac{\ln(\tau_n^P/\tau_n^S)}{\sqrt{2}\sigma_P} \right) \right\} \right] \\ J_2(\tau_n^S) & = & J_U \dfrac{\pi}{2} \left[A_B(\tau_n^S)^\alpha + A_P \exp\left(-\dfrac{(\ln(\tau_n^P/\tau_n^S))^2}{2\sigma_P^2} \right) \right] + J_U \tau_n^S, \end{array} \right. \tag{3.5}$$

where $\tau_n^S = \tau_S/(2\pi\tau_M)$ represents the normalized period of the seismic wave with period τ_S. Shear wave velocity and attenuation are calculated from J_1 and J_2 as

$$\left\{ \begin{array}{rcll} V_S & = & \dfrac{1}{\sqrt{\rho J_1}} \left(\dfrac{1 + \sqrt{1 + (J_2/J_1)^2}}{2} \right)^{-\frac{1}{2}} & \simeq \dfrac{1}{\sqrt{\rho J_1}} \\ Q_S^{-1} & = & \dfrac{J_2}{J_1} \left(\dfrac{1 + \sqrt{1 + (J_2/J_1)^2}}{2} \right)^{-1} & \simeq \dfrac{J_2}{J_1}. \end{array} \right. \tag{3.6}$$

The unrelaxed compliance $J_U = 1/\mu_U$ is written as $J_U = J_U(P,T) \times (1 + \Delta_{\mathrm{poro}}(\phi))$ by taking into account the modulus reduction by the poroelastic effect, where melt follows the undrained condition in the seismic waves. When ϕ is very small, $\Delta_{\mathrm{poro}} \simeq 0$ and $J_U = J_U(P,T)$.

The Maxwell relaxation time τ_M is written as $\tau_M = \eta/\mu_U$ with unrelaxed shear modulus μ_U and shear viscosity η, which is given by

$$\eta = \eta_r \left(\frac{d}{d_r} \right)^m \exp\left[\frac{H}{R} \left(\frac{1}{T} - \frac{1}{T_r} \right) \right] \exp\left[\frac{V}{R} \left(\frac{P}{T} - \frac{P_r}{T_r} \right) \right] A_\eta(T_n), \tag{3.7}$$

Table 3.1: Parameter Values

Parameter	Value[a]
A_B	0.664
α	0.38
τ_n^P	6×10^{-5}
$\beta(\phi)$	~ 0[b]
$\Delta_{\rm poro}(\phi)$	~ 0[b]
γ	5
T_n^η	0.94
$\lambda\phi$	~ 0[b]

[a] Based on the data of #41.
[b] Here direct effects of melt are not taken into account.

where η_r represents a reference shear viscosity for reference temperature T_r, reference pressure P_r, and reference grain size d_r, m is grain size exponent, H is activation energy, V is activation volume, and R is the gas constant. The last factor $A_\eta(T_n)$ in (3.7) is introduced to take into account the extra reduction just below the solidus temperature. We define $A_\eta(T_n)$ as

$$A_\eta(T_n) = \begin{cases} 1 & \text{at } T_n < T_n^\eta \\ \exp\left[-\dfrac{(T_n - T_n^\eta)}{(T_n - T_n T_n^\eta)} \ln\gamma\right] & \text{at } T_n^\eta \le T_n < 1 \\ \gamma^{-1}\exp\left(-\lambda\phi\right) & \text{at } 1 \le T_n, \end{cases} \tag{3.8}$$

where $\gamma(\ge 1)$ represents the factor of the extra reduction and T_n^η represents the normalized temperature above which the activation energy is higher than H. Let $H+\Delta H$ be the high activation energy at $T_n^\eta \le T_n \le 1$. Then, the three parameters γ, T_n^η, and ΔH satisfy the relationship $\Delta H = RT_mT_n^\eta(1-T_n^\eta)^{-1}\ln\gamma$, showing that only two of the three are independent. The direct effect of melt is also introduced into $A_\eta(T_n)$ by the exponential factor $\exp(-\lambda\phi)$, which approaches one as ϕ approaches zero.

3.2 Applicability to the Mantle

The new anelasticity model given by equations (3.5) with (3.3) and (3.4), and the new viscosity model given by equations (3.7) and (3.8) were fitted to the seismic velocity data of the Pacific mantle at 50 and 75 km depths obtained by *Priestley and McKenzie* [2013] (hereafter called PM2013) as a function of temperature. The parameter values of the anelasticity model used in the analysis are given in Table 3.1, which are faithful to the present experimental data. As shown in this table, the direct effects of the melt phase

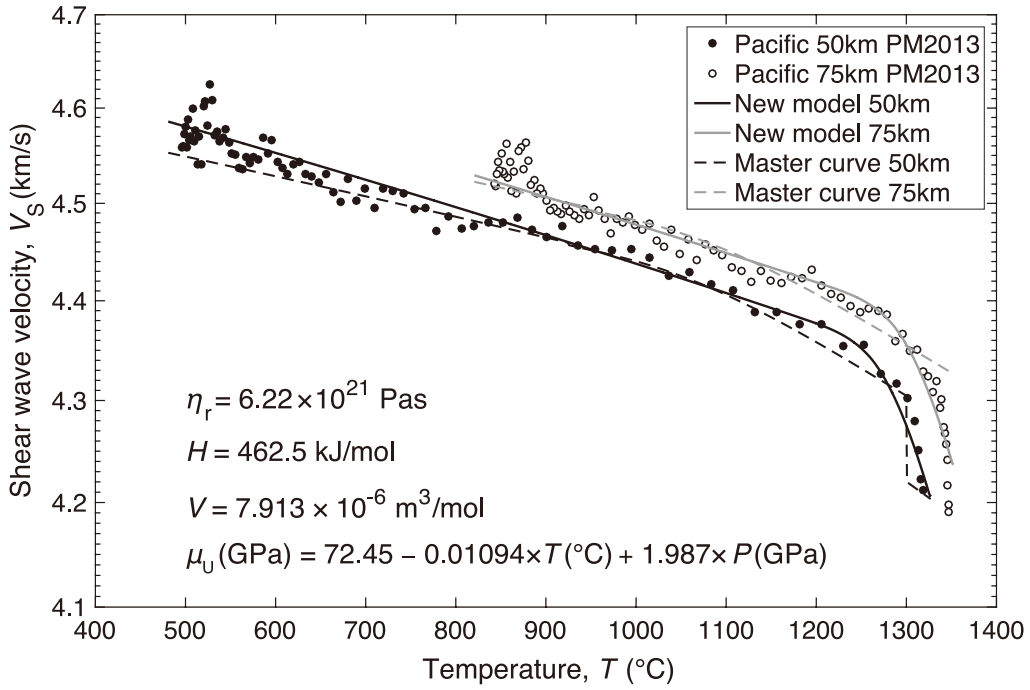

Figure 3.2: The new anelasticity model proposed in this study was fitted to the velocity profiles of the Pacific mantle obtained by *Priestley and McKenzie* [2013] (PM2013). Also shown are the previous fits by using the master curve model proposed by *McCarthy et al.* [2011]. The six of the seven fitting parameters (reference viscosity η_r for $T_r = 1200$°C, $P_r = 1.5$ GPa, and $d_r = d$, activation energy H, activation volume V, unrelaxed shear modulus μ_U^0 at 0°C and 0 Pa, $\partial\mu_U/\partial T$, and $\partial\mu_U/\partial P$) determined by the inversion are shown in the lower left. Also, T_m at 75 km depth was determined as 1351°C, where T_m at 50 km depth was fixed to 1326°C. The fitting parameters for the master curve model are presented in Table 1 of PM2013 (thick letters).

are neglected in this analysis because melt fraction is considered to be small ($\ll 1\%$) in most of this region [e.g., *Hirschmann*, 2010]. Following PM2013, the material parameters of the mantle rock needed to calculate the seismic velocity (μ_U^0 at 0°C and 0 Pa, $\partial\mu_U/\partial T$, and $\partial\mu_U/\partial P$ for elasticity; η_r at $T_r = 1200$°C, $P_r = 1.5$ GPa, and $d_r = d$, H, and V for viscosity; $T_m(75\text{ km}) - T_m(50\text{ km})$ for solidus) were determined by the fitting of the anelasticity model to the geophysical constraints. We used the same program and constraints as PM2013 presented in section 4 of PM2013. We can check the applicability of the new anelasticity model to the mantle data by comparing the values of parameters determined by the fitting with those measured in laboratory and investigating whether they agree well. The solidus temperature at 50 km depth was assumed to be 1326°C (dry solidus at $P = 1.67$ GPa).

The result of the fitting is shown in Figure 3.2, together with the previous result of PM2013 by using the master curve model. As shown in this figure, the new model explains well the temperature dependence of V_S in the oceanic lithosphere, particularly

the steep reduction just below the solidus temperature, which was difficult to explain by the previous model. Shown in the lower left are the fitting parameters determined for the new model, which are consistent with those experimentally measured for olivine aggregates (Table 1 of PM2013). The good agreement indicates the applicability of the new anelasticity model to the mantle. Although the anelastic effect at 50 km depth starts at about 950°C in the previous model, it starts at 1200°C in the new model. The steep reduction in V_S occurs because temperature is just below the solidus temperature, and whether very small amount of melt exists or not does not matter in this model. Here, I note that the analysis in section 3.1 by using the experimental data and the fitting in section 3.2 to the seismological data were performed independently, by myself and by co-author Y. Takei of *Yamauchi and Takei* [2016], respectively, so that the applicability of the present empirical model to the mantle can be examined strictly. Further details of the fitting and its seismological implications are presented by *Takei* [2017].

Takei [2017] pointed out that in the new anelasticity model, besides temperature and partial melting, volatiles (H_2O and CO_2) play an important role. For example, the solidus temperature at 75 km depth determined by the fitting (1351°C) is considerably lower than the dry peridotite solidus (1436°C). This result can be interpreted that the solidus temperature is depressed by volatiles existing at 75 km depth.

The geophysical application in this section was concerned with the temperature gradient of V_S, $\partial V_S/\partial T$. The application in the next chapter is concerned with the spatial gradient of V_S, $\partial V_S/\partial z$, which further depends on the spatial gradient of temperature, $\partial T/\partial z$, and that of solidus, $\partial T_m/\partial z$, which is affected by volatile distribution.

Chapter 4

Origin of the Lithosphere-Asthenosphere Boundary

本章については、５年以内に雑誌などで刊行予定のため、非公開。

Chapter 5

Conclusions

I measured elasticity, anelasticity, and viscosity of a polycrystalline aggregate at near-solidus temperatures ranging from subsolidus to supersolidus temperatures (Chapter 2). Effects of "partial melting" on the mechanical properties captured in this study are twofold; changes just before the solidus temperature ($0.92 \sim< T/T_m < 1$) in the absence of melt and changes at the solidus temperature ($T = T_m$) due to the onset of partial melting. As temperature increases from $T \simeq 0.92T_m$ to T_m, the amplitude and width of the high-frequency peak X_P gradually increase, causing a breakdown of the Maxwell frequency scaling for anelasticity at high normalized frequencies ($f/f_M \geq 10^4$). In addition, viscosity reduction by temperature shows a higher activation energy at $T/T_m \geq 0.94$ than at $T/T_m < 0.94$. At $T = T_m$, further reduction of elasticity due to the poroelastic effect, further increase of the amplitude of X_P, and further reduction of viscosity by a factor of $e^{-\lambda\phi}$ ($\lambda > 0$) occur.

The changes in anelasticity and viscosity just below the solidus temperature are caused by a solid state mechanism, whereas the changes at the solidus temperature are caused by the direct effects of the melt phase. The grain size exponent of viscosity is almost 3, showing that the mechanism is the grain boundary diffusion creep. The mechanism of the high-frequency peak X_P is considered to be the diffusionally accommodated grain boundary sliding, which is equal to the mechanism of the background X_B. This is supported by the facts that the center position of X_P follows the Maxwell frequency scaling and that under the strong hysteresis, X_P fully follows the Maxwell frequency scaling. The hysteresis, which was newly recognized in this study, shows that the behavior of X_P is closely related to the partial melting. I speculate that a structural transition of grain boundary by premelting occurs just below the solidus temperature and enhances

the matter diffusion along the grain boundary.

The changes by the premelting effect are not sensitive to the concentration of the secondary component (diphenylamine), and even when samples generate very small amounts of melt (0.4–0.54%) at $T = T_m$, the amplitude of these changes is large. In contrast, the changes by the direct effect of melt depend on the melt fraction and the amplitude is very small when the samples have very small melt fractions ($< 1\%$). In most parts of the upper mantle, melt fraction is considered to be very small ($\ll 1\%$). In these regions, it is predicted that the direct effect of melt is negligibly small, and the mechanical properties are determined by the premelting effect.

The parameterization of the experimental results was performed in section 3.1. The obtained empirical formula was fitted to the temperature dependence of the seismic wave velocity in the Pacific mantle obtained by *Priestley and McKenzie* [2013] (section 3.2). The steep reduction of $V_S(T)$ just below the solidus temperature near the ridge can be explained well by the premelting effect without any direct effects of melt. In this fitting, the material parameters for the viscosity and elasticity of the mantle rock, which are needed to calculate the Maxwell relaxation time, are determined as the fitting parameters. The obtained fitting parameters agree well with those experimentally measured for the olivine aggregates. By combining the empirical formula (section 3.1) and the material parameters determined by the fitting (section 3.2), the new anelasticity model applicable to the mantle is completed.

In Chapter 4, I further applied the new anelasticity model to the oceanic lithosphere-asthenosphere boundary (LAB) to investigate whether the premelting effect can explain the seismic discontinuity. The vertical structure of V_S was calculated by using the geotherm obtained from the cooling models of oceanic plate and the solidus temperature of peridotite obtained from the thermodynamic models. I found that if the solidus temperature is decreased by the existence of volatile (water), the steep reduction of $V_S(z)$ (seismic discontinuity) can be reproduced by the premelting effect. In addition, the premelting effect could explain the high attenuation and the weak dependency of attenuation on frequency in the asthenosphere. I propose a new hypothesis that the asthenosphere is caused by the premelting effect. Although some difficulty remains in the quantitative explanation for the amplitude of seismic discontinuity (ΔV_S), the present results are not conclusive and it could be solved by the further refinement of the model on the basis

of future experimental and theoretical studies. It is especially important to clarify the material dependence of the premelting phenomenon and detailed behavior of premelting (disordering) for $T/T_m > 1$.

Temperature, volatile, and "partial melting" work not independently but mutually to cause premelting. This point is a distinctive difference of the present anelasticity model from the existing models. With the premelting effect, interpretation of the seismic structures will change significantly. In particular, melt fraction needed to explain low V and/or high Q^{-1} will become considerably smaller than that interpreted by using only the direct effects of melt. Toward the application of the new model to the places where melt fraction is considered to be large (e.g., volcanic fronts), I am planning a further experimental study to investigate the dependency of X_P on melt fraction ($> 1\%$) and the effect of the formation of melt network on anelasticity and viscosity.

Appendix

A Plots of $E(f)$ and $Q^{-1}(f)$ for Samples #40, 44, and 43

Figure A.1 shows the results of the forced oscillation tests for samples #40, 44, and 43 as functions of frequency. In Figures A.1a–d, the data from the repeated run are also plotted (open symbols at $T/T_m < 1$ and solid symbols at $T/T_m > 1$); the good reproducibility can be confirmed from the agreement between the primary and repeated runs. Although the data from the repeated run are not shown in the other plots in the text and in Figure A.1, the good reproducibility similar to these two samples was obtained for all samples.

B Comparison Between X_P and the Gaussian Distribution (#41)

In Figure B.1, symbols show the data of X_P for sample #41, and lines show the Gaussian distributions determined by fitting to these data (solid) and by additionally using the modulus data (dashed). The data at low temperatures ($T \leq 29$°C) are fitted fairly well by the Gaussian distribution (solid line). Using the data at $T \leq 29$°C, we also confirmed the consistency between Δ_P determined from X_P and Δ_P determined from modulus data, as shown in Figure 2.16d (black and gray squares). At $T \geq 35$°C, although the data points exist only on the longer time scale side of the peak, we determined Δ_P and σ_P by using the modulus data and the constant value of τ_P/τ_M determined at $T \leq 29$°C (dashed line).

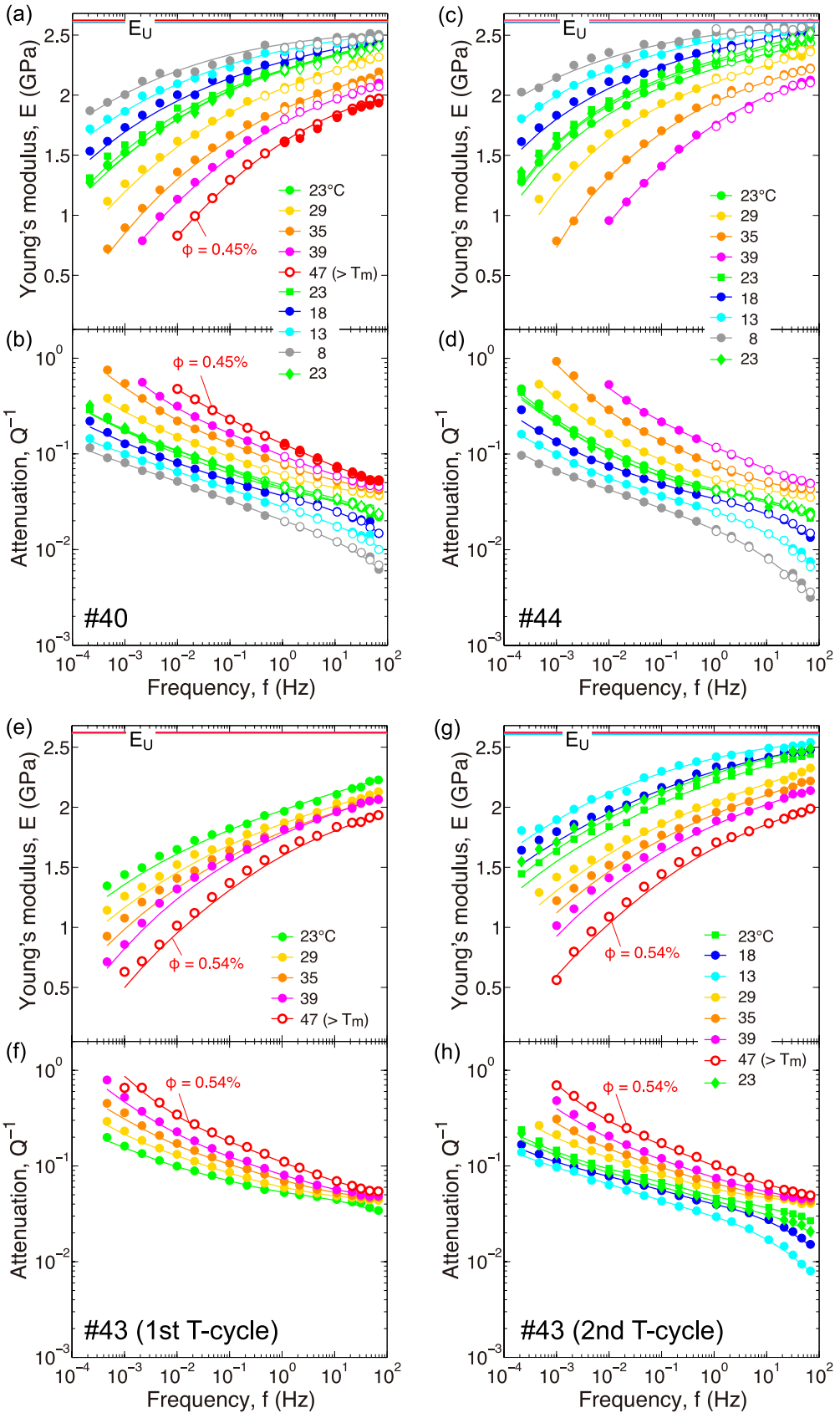

Figure A.1: Young's modulus and attenuation versus frequency. (a, b) Sample #40, (c, d) #44, (e, f) #43 in the first temperature cycle, and (g, h) #43 in the second temperature cycle. Explanations for color, symbol type, line, and order of legend are given in the caption of Figure 2.10. In Figures A.1a–d, data from the repeated run are also plotted by using open symbols at $T < T_m$ and solid symbols at $T > T_m$ to demonstrate the good reproducibility.

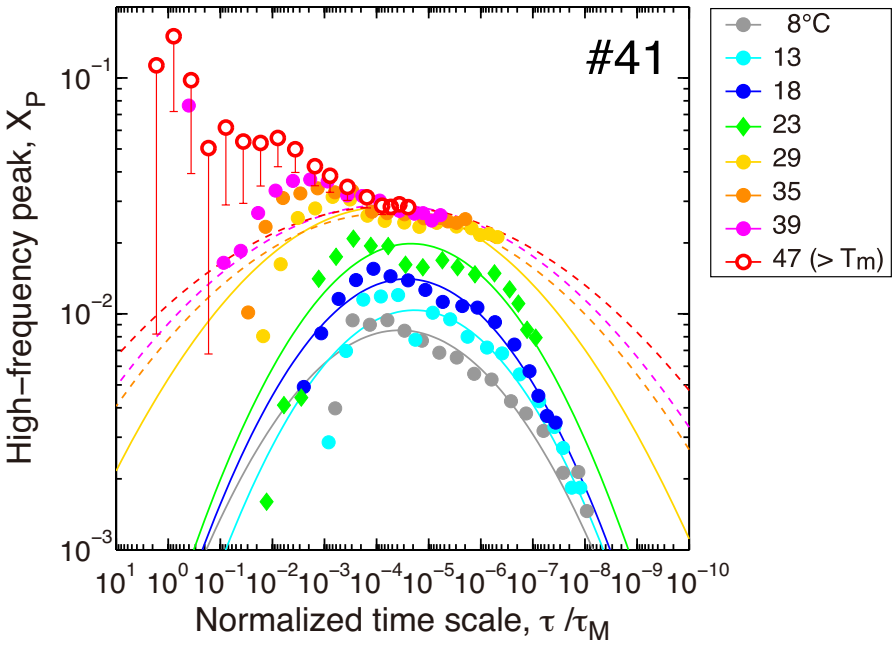

Figure B.1: High-frequency peak X_P for sample #41 (symbols). Lines show the Gaussian distribution determined by the fitting to these X_P data (solid) and by additionally using the modulus data (dashed).

Acknowledgments

I am deeply grateful to my supervisor, Prof. Yasuko Takei for the continuing guidance and encouragement. Her advice always stimulated me to challenge new experiments or calculations. I also thank Assoc. Prof. Takehiko Hiraga very much for frequent, stimulating and helpful discussions. I would like to give thanks to the defence committee members: Prof. Hitoshi Kawakatsu, Assoc. Prof. Masao Nakatani, and Assoc. Prof. Kenji Kawai. Their constructive comments were very helpful to improve this thesis.

I would like to thank Mr. Masayuki Uchida, Mr. Akio Kaneko, and Mr. Minoru Sakaue for technical assistance and Assoc. Prof. Atsushi Yasuda for allowing me to access the microscope. A portion of Chapter 1 and main portions of Chapters 2–3 are based on the original paper *Yamauchi and Takei* [2016], and we especially thank Prof. Dan McKenzie, who provided the program and data used in the fitting in section 3.2.

Also, I thank Dr. Akihiro Takeuchi, Dr. Kenta Ueki, and the members of Takei and Hiraga laboratories (Dr. Ayako Suzuki, Dr. Sanae Koizumi, Dr. Akira Shimojuku, Mr. Tadashi Nakakoji, Mr. Kenta Sueyoshi, Mr. Genta Maruyama, Mr. Kosuke Yabe, Mr. Yuto Sasaki, and Mr. Atsuro Okamoto) for fruitful discussions in the seminar and for their kindness in the daily life.

Bibliography

[1] Abers, G. A., K. M. Fischer, G. Hirth, D. A. Wiens, T. Plank, B. K. Holtzman, C. McCarthy, and E. Gazel (2014), Reconciling mantle attenuation-temperature relationships from seismology, petrology, and laboratory measurements, *Geochem. Geophys. Geosyst.*, *15*, 3521–3542, doi:10.1002/2014GC005444.

[2] Anderson, D. L. (1989), *Theory of the Earth*, Blackwell Scientific Publications, Boston.

[3] Anderson, D. L., and J. W. Given (1982), Absorption band Q model for the Earth, *J. Geophys. Res.*, *87*(B5), 3893–3904, doi:10.1029/JB087iB05p03893.

[4] Asimow, P. D., J. E. Dixon, and C. H. Langmuir (2004), A hydrous melting and fractionation model for mid-ocean ridge basalts: Application to the Mid-Atlantic Ridge near the Azores, *Geochem. Geophys. Geosyst.*, *5*, Q01E16, doi:10.1029/2003GC000568.

[5] Bagley, B., and J. Revenaugh (2008), Upper mantle seismic shear discontinuities of the Pacific. *J. Geophys. Res.*, *113*, B12301, doi:10.1029/2008JB005692.

[6] Barnhoorn, A., I. Jackson, J. D. Fitz Gerald, and Y. Aizawa (2007), Suppression of elastically accommodated grain-boundary sliding in high-purity MgO, *J. Eur. Ceram. Soc.*, *27*, 4697–4703.

[7] Biot, M. A. (1956), Theory of propagation of elastic waves in a fluid-saturated porous solid. I. Low-frequency range, *J. Acoust. Soc. Am.*, *28*, 168–178.

[8] Cantwell, P. R., M. Tang, S. J. Dillon, J. Luo, G. S. Rohrer, and M. P. Harmer (2014), Grain boundary complexions, *Acta Materialia*, *62*, 1–48.

[9] Cleary, M. P. (1978), Elastic and dynamic response regimes of fluid-impregnated solids with diverse microstructures, *Int. J. Solids Struct.*, *14*, 795–819.

[10] Cooper, R. F., D. L. Kohlstedt, and K. Chyung (1989), Solution-precipitation enhanced creep in solid-liquid aggregates which display a non-zero dihedral angle, *Acta Metall.*, *37*, 1759–1771.

[11] D'Ans, J., D. Jänchen, E. Kaufmann, and C. Kux (Eds) (1964), *Landolt-Börnstein Zahlenwerte und Funktionen aus Physik, Chemie, Astronomie, Geophysik, und Technik*, II-2c, Lösungsgleichgewichte II, Springer-Verlag, Berlin.

[12] Dasgupta, R., and M. M. Hirschmann (2010), The deep carbon cycle and melting in Earth's interior, *Earth Planet. Sci. Lett.*, *298*, 1–13.

[13] Dasgupta, R., M. M. Hirschmann, and N. D. Smith (2007), Water follows carbon: CO2 incites deep silicate melting and dehydration beneath mid-ocean ridges, *Geology*, *35(2)*, 135–138.

[14] Dasgupta, R., A. Mallik, K. Tsuno, A. C. Withers, G. Hirth, and M. M. Hirschmann (2013), Carbon-dioxide-rich silicate melt in the Earth's upper mantle, *Nature*, *493*, 211–215.

[15] Deuss, A., and J. H. Woodhouse (2004), The nature of the Lehmann discontinuity from its seismological Clapeyron slopes, *Earth Planet. Sci. Lett.*, *225*, 295–304.

[16] Duffy, T. S., and D. L. Anderson (1989), Seismic velocities in mantle minerals and the mineralogy of the upper mantle, *J. Geophys. Res.*, *94*(B2), 1895–1912, doi:10.1029/JB094iB02p01895.

[17] Dziewonski, A. M., and D. L. Anderson (1981), Preliminary reference Earth model, *Phys. Earth Planet. Inter.*, *25*, 297–356.

[18] Faul, U., and I. Jackson (2015), Transient creep and strain energy dissipation: An experimental perspective, *Annu. Rev. Earth Planet. Sci.*, *43*, 541–569.

[19] Fischer, K. M., H. A. Ford, D. L. Abt, amd C. A. Rychert (2010), The lithosphere-asthenosphere boundary, *Annual Review of Earth and Planetary Sciences*, *38*, 551–575.

[20] Gaherty, J. B., M. Kato, and T. H. Jordan (1999), Seismological structure of the upper mantle: a regional comparison of seismic layering. *Phys. Earth Planet. Inter.*, *110*, 21–41.

[21] Garapić, G., U. H. Faul, and E. Brisson (2013), High-resolution imaging of the melt distribution in partially molten upper mantle rocks: evidence for wetted two-grain boundaries. *Geochem. Geophys. Geosyst.*, *14*, 556–566, doi:10.1029/2012GC004547.

[22] Ghiorso, M. S., M. M. Hirschmann, P. W. Reiners, and V. C. Kress III (2002), The pMELTS: A revision of MELTS for improved calculation of phase relations and major element partitioning related to partial melting of the mantle to 3 GPa, *Geochem. Geophys. Geosyst.*, *3*(5), 10.1029/2001GC000217, 2002.

[23] Gifkins, R. C. (1970), *Optical Microscopy of Metals*, Elsevier, New York.

[24] Gribb, T. T., and R. F. Cooper (1998), Low-frequency shear attenuation in polycrystalline olivine: Grain boundary diffusion and the physical significance of the Andrade model for viscoelastic rheology, *J. Geophys. Res.*, *103*(B11), 27267–27279, doi:10.1029/98JB02786.

[25] Gutenberg, B. (1959), *Physics of the Earth's Interior*, Academic Press, New York.

[26] Hirschmann, M. M. (2010), Partial melt in the oceanic low velocity zone, *Phys. Earth Planet. Inter.*, *179*, 60–71.

[27] Hirschmann, M. M., T. Tenner, C. Aubaud, and A. C. Withers (2009), Dehydration melting of nominally anhydrous mantle: The primacy of partitioning, *Phys. Earth Planet. Inter.*, *176*, 54–68.

[28] Hirth, G. and D. Kohlstedt (2003), Rheology of the upper mantle and the mantle wedge: A view from the experimentalists, in *Inside the Subduction Factory, Geophys. Monogr. Ser.*, vol. 138, edited by J. Eiler, pp. 83–105, AGU, Washington, D. C.

[29] Holness, M. B. (1997), Surface chemical controls on pore-fluid connectivity in texturally equilibrated materials, in *Fluid flow and transport in rocks*, edited by B. Jamtveit and B. Yardley, pp. 149–169, Chapman and Hall, London.

[30] Holtzman, B. K. (2016), Questions on the existence, persistence, and mechanical effects of a very small melt fraction in the asthenosphere, *Geochem. Geophys. Geosyst.*, *17*, 470–484, doi:10.1002/2015GC006102.

[31] Isaak, D. G. (1992), High-temperature elasticity of iron-bearing olivines, *J. Geophys. Res.*, *97*, 1871–1885.

[32] Jackson, I. (2015), Properties of rocks and minerals: Physical origins of anelasticity and attenuation in rock, in *Treatise on Geophysics*, 2nd ed., edited by G. Schubert, pp. 539–571, Elsevier, Amsterdam.

[33] Jackson, I., and U. H. Faul (2010), Grainsize-sensitive viscoelastic relaxation in olivine: Towards a robust laboratory-based model for seismological application, *Phys. Earth Planet. Inter.*, *183*, 151–163.

[34] Jackson, I., J. D. Fitz Gerald, U. H. Faul, and B. H. Tan (2002), Grain-size-sensitive seismic wave attenuation in polycrystalline olivine, *J. Geophys. Res.*, *107*(B12), 2360, doi:10.1029/2001JB001225.

[35] Jackson, I., U. H. Faul, J. D. Fitz Gerald, and B. H. Tan (2004), Shear wave attenuation and dispersion in melt-bearing olivine polycrystals: 1. Specimen fabrication and mechanical testing, *J. Geophys. Res.*, *109*, B06201, doi:10.1029/2003JB002406.

[36] Karato, S. (1992), On the Lehmann discontinuity, *Geophys. Res. Lett.*, *19*(22), 2255–2258.

[37] Karato, S. (1993), Importance of anelasticity in the interpretation of seismic tomography, *Geophys. Res. Lett.*, *20*(15), 1623–1626, doi:10.1029/93GL01767.

[38] Karato, S. (2008), *Deformation of earth materials: an introduction to the rheology of solid earth*, Cambridge University Press, Cambridge.

[39] Karato, S (2012), On the origin of the asthenosphere, *Earth Planet. Sci. Lett.*, *321–322*, 95–103.

[40] Kawakatsu, H., P. Kumar, Y. Takei, M. Shinohara, T. Kanazawa, E. Araki, and K. Suyehiro (2009), Seismic evidence for sharp lithosphere-asthenosphere boundaries of oceanic plates. *Science*, *324*(5926), 499–502.

[41] Kumar, P., and H. Kawakatsu (2011), Imaging the seismic lithosphere - asthenosphere boundary of the oceanic plate, *Geochem., Geophys., Geosyst.*, *12*, Q01006, doi:10.1029/2010GC003358.

[42] Lehmann, I. (1961), S and the structure of the upper mantle, *Geophys. J. Roy. Astron. Soc.*, *4*, 124–138.

[43] Lu, C., and I. Jackson (2006), Low-frequency seismic properties of thermally cracked and argon-saturated granite, *Geophysics*, *71*(6), F147–F159.

[44] Maruyama, G., and T. Hiraga (2017), Grain- to multiple-grain-scale deformation processes during diffusion creep of forsterite + diopside aggregate: 2. Grain boundary sliding-induced grain rotation and its role in crystallographic preferred orientation in rocks, *J. Geophys. Res. Solid Earth*, *122*, 5916–5934, doi:10.1002/2017JB014255.

[45] Mavko, G., and A. Nur (1975), Melt squirt in the asthenosphere, *J. Geophys. Res.*, *80*, 1444–1448, doi:10.1029/JB080i011p01444.

[46] McCarthy, C., and Y. Takei (2011), Anelasticity and viscosity of partially molten rock analogue: Toward seismic detection of small quantities of melt, *Geophys. Res. Lett.*, *38*, L18306, doi:10.1029/2011GL048776.

[47] McCarthy, C., Y. Takei, and T. Hiraga (2011), Experimental study of attenuation and dispersion over a broad frequency range: 2. The universal scaling of polycrystalline materials, *J. Geophys. Res.*, *116*, B09207, doi:10.1029/2011JB008384.

[48] McKenzie, D. (1985), The extraction of magma from the crust and mantle, *Earth Planet. Sci. Lett.*, *74*, 81–91.

[49] McKenzie, D. (2000), Constraints on melt generation and transport from U-series activity ratios, *Chemical Geology*, *162*, 81–94.

[50] McKenzie, D., and M. J. Bickle (1988), The volume and composition of melt generated by extension of the lithosphere, *Journal of petrology*, *29(3)*, 625–679.

[51] McKenzie, D., J. Jackson, and K. Priestley (2005), Thermal structure of oceanic and continental lithosphere, *Earth Planet. Sci. Lett.*, *233*, 337–349.

[52] Mei, S., and D. L. Kohlstedt (2000), Influence of water on plastic deformation of olivine aggregates: 1. Diffusion creep regime, *J. Geophys. Res.*, *105*, 21457–21469.

[53] Mei, S., W. Bai, T. Hiraga, and D. L. Kohlstedt (2002), Influence of melt on the creep behavior of olivine-basalt aggregates under hydrous conditions. *Earth Planet. Sci. Lett.*, *201*, 491–507.

[54] Mierdel, K., H. Keppler, J. R. Smyth, and F. Langenhorst (2007), Water solubility in aluminas orthopyroxene and the origin of Earth's asthenosphere, *Science*, *315*, 364–368.

[55] Miyazaki, T., K. Sueyoshi, and T. Hiraga (2013), Olivine crystals align during diffusion creep of Earth's upper mantle, *Nature*, *502(7471)*, 321–326.

[56] Morris, S. J. S., and I. Jackson (2009), Implications of the similarity principle relating creep and attenuation in finely grained solids, *Mater. Sci. Eng. A*, *521–522*, 124–127.

[57] Nakajima, J., Y. Takei, and A. Hasegawa (2005), Quantitative analysis of the inclined low-velocity zone in the mantle wedge of northeastern Japan: A systematic change of melt-filled pore shapes with depth and its implications for melt migration, *Earth Planet. Sci. Lett.*, *234*, 59–70.

[58] Nakajima, J., S. Hada, E. Hayami, N. Uchida, A. Hasegawa, S. Yoshioka, T. Matsuzawa, and N. Umino (2013), Seismic attenuation beneath northeastern Japan: Constraints on mantle dynamics and arc magmatism, *J. Geophys. Res.*, *118*, 5838–5855, doi:10.1002/2013JB010388.

[59] Nowick, A. S., and B. S. Berry (1972), *Anelastic Relaxation in Crystalline Solids*, Academic Press, San Diego, Calif.

[60] Parsons, B., and J. G. Sclater (1977), An analysis of the variation of ocean floor bathymetry and heat flow with age, *J. Geophys. Res.*, *82*, 803-827.

[61] Priestley, K., and D. McKenzie (2006), The thermal structure of the lithosphere from shear wave velocities, *Earth Planet. Sci. Lett.*, *244*, 285–301.

[62] Priestley, K., and D. McKenzie (2013), The relationship between shear wave velocity, temperature, attenuation and viscosity in the shallow part of the mantle, *Earth Planet. Sci. Lett.*, *381*, 78–91.

[63] Putirka, K. D. (2005), Mantle potential temperatures at Hawaii, Iceland, and the mid -ocean ridge system, as inferred from olivine phenocrysts: Evidence for thermally driven mantle plumes, *Geochem. Geophys. Geosyst.*, *6*, Q05L08, doi:10.1029/ 2005GC000915.

[64] Raj, R. (1975), Transient behavior of diffusion-induced creep and creep rupture, *Metall. Trans.*, *6A*, 1499–1509.

[65] Raj, R., and M. F. Ashby (1971), On grain boundary sliding and diffusional creep, *Metall. Trans.*, *2*, 1113–1127.

[66] Rychert, C. A., and P. M. Shearer (2011), Imaging the lithosphere-asthenosphere boundary beneath the Pacific using SS waveform modeling, *J. Geophys. Res.*, *116*, B07307, doi:10.1029/2010JB008070.

[67] Sakurai, M., N. Tsujino, H. Sakuma, K. Kawamura, and E. Takahashi (2014), Effects of Al content on water partitioning between orthopyroxene and olivine: Implications for lithosphere-asthenosphere boundary, *Earth Planet. Sci. Lett.*, *400*, 284–291.

[68] Salters, V. J. M., and A. Stracke (2004), Composition of the depleted mantle, *Geochem. Geophys. Geosyst.*, *5*, Q05B07, doi:10.1029/2003GC000597.

[69] Schmerr, N. (2012). The Gutenberg discontinuity: Melt at the lithosphere-asthenosphere boundary, *Science*, *335(6075)*, 1480–1483.

[70] Sherwood, J. N. (1979), Lattice defects, self-diffusion, and the plasticity of plastic crystals, in *The Plastically Crystalline State*, edited by J. N. Sherwood, pp. 39–83, Wiley Intersci., New York.

[71] Smith, P. M., and P. D. Asimow (2005), Adiabat_1ph: A new public front-end to the MELTS, pMELTS, and pHMELTS models, *Geochem. Geophys. Geosyst.*, *6*, Q02004, doi:10.1029/2004GC000816.

[72] Stein, C. A., and S. Stein (1992), A model for the global variation in oceanic depth and heat flow with lithospheric age, *Nature*, *359*, 123–129.

[73] Sundberg, M., and R. F. Cooper (2010), A composite viscoelastic model for incorporating grain boundary sliding and transient diffusion creep; correlating creep and attenuation responses for materials with a fine grain size, *Philos. Mag.*, *90*, 2817–2840.

[74] Takei, Y. (1998), Constitutive mechanical relations of solid-liquid composites in terms of grain-boundary contiguity, *J. Geophys. Res.*, *103*(B8), 18183–18203, doi:10.1029/98JB01489.

[75] Takei, Y. (2000), Acoustic properties of partially molten media studied on a simple binary system with a controllable dihedral angle, *J. Geophys. Res.*, *105*(B7), 16665–16682, doi:10.1029/2000JB900124.

[76] Takei, Y. (2002), Effect of pore geometry on V_P/V_S: From equilibrium geometry to crack, *J. Geophys. Res.*, *107*(B2), 2043, doi:10.1029/2001JB000522.

[77] Takei, Y. (2017), Effects of partial melting on seismic velocity and attenuation: A new insight from experiments, *Annual Review of Earth and Planetary Sciences*, *45*, 447–470.

[78] Takei, Y., and B. K. Holtzman (2009a), Viscous constitutive relations of solid-liquid composites in terms of grain boundary contiguity: 1. Grain boundary diffusion control model, *J. Geophys. Res.*, *114*, B06205, doi:10.1029/2008JB005850.

[79] Takei, Y., and B. K. Holtzman (2009b). Viscous constitutive relations of solid-liquid composites in terms of grain boundary contiguity: 2. Compositional model for small melt fractions, *J. Geophys. Res.*, *114*, B06206, doi:10.1029/2008JB005851.

[80] Takei, Y., K. Fujisawa, and C. McCarthy (2011), Experimental study of attenuation and dispersion over a broad frequency range: 1. The apparatus, *J. Geophys. Res.*, *116*, B09204, doi:10.1029/2011JB008382.

[81] Takei, Y., F. Karasawa, and H. Yamauchi (2014), Temperature, grain size, and chemical controls on polycrystal anelasticity over a broad frequency range extending into the seismic range, *J. Geophys. Res. Solid Earth*, *119*, 5414–5443, doi:10.1002/2014JB011146.

[82] Takeuchi, N., H. Kawakatsu, H. Shiobara, T. Isse, H. Sugioka, A. Ito, and H. Utada (2017), Determination of intrinsic attenuation in the oceanic lithosphere-asthenosphere system, *Science*, *358*(6370), 1593–1596.

[83] Tan, B. H., I. Jackson, and J. D. Fitz Gerald (2001), High-temperature viscoelasticity of fine-grained polycrystalline olivine, *Phys. Chem. Miner.*, *28*, 641–664, doi:10.1007/s002690100189.

[84] Turcotte, D., and G. Schubert (2014), *Geodynamics*, 3rd ed., Cambridge University Press, Cambridge.

[85] Webb, S., and I. Jackson, (2003), Anelasticity and microcreep in polycrystalline MgO at high temperature: an exploratory study, *Phys. Chem. Miner.*, *30*, 157–166, doi:10.1007/s00269-003-0299-1.

[86] Wolf, D. (2001), High-temperature structure and properties of grain boundaries: long-range vs. short-range structural effects, *Curr. Opin. Solid State Mater. Sci.*, *5*, 435–443.

[87] Workman, R. K., and S. R. Hart (2005), Major and trace element composition of the depleted MORB mantle (DMM), *Earth Planet. Sci. Lett.*, *231*, 53–72.

[88] Yabe, K., and T. Hiraga (2017), Diffusional creep of fine-grained olivine aggregates; Chemical and melt effects, Abstract [MR24B-02] presented at 2017 Fall Meeting, AGU, New Orleans, LA, 11–15 Dec.

[89] Yamauchi, H., and Y. Takei (2016), Polycrystal anelasticity at near-solidus temperatures, *J. Geophys. Res. Solid Earth*, *121*, 7790–7820, doi:10.1002/2016JB013316.

[90] Zhao, Y. H., S. B. Ginsberg, and D. L. Kohlstedt (2004), Solubility of hydrogen in olivine: dependence on temperature and iron content, *Contributions to Mineralogy and Petrology*, *147*, 155–161.

[91] Zimmerman, M. E., and D. L. Kohlstedt (2004), Rheological properties of partially molten lherzolite, *J. Petrol.*, *45*(2), 275–298.